



저작자표시-비영리-변경금지 2.0 대한민국

이용자는 아래의 조건을 따르는 경우에 한하여 자유롭게

- 이 저작물을 복제, 배포, 전송, 전시, 공연 및 방송할 수 있습니다.

다음과 같은 조건을 따라야 합니다:



저작자표시. 귀하는 원저작자를 표시하여야 합니다.



비영리. 귀하는 이 저작물을 영리 목적으로 이용할 수 없습니다.



변경금지. 귀하는 이 저작물을 개작, 변형 또는 가공할 수 없습니다.

- 귀하는, 이 저작물의 재이용이나 배포의 경우, 이 저작물에 적용된 이용허락조건을 명확하게 나타내어야 합니다.
- 저작권자로부터 별도의 허가를 받으면 이러한 조건들은 적용되지 않습니다.

저작권법에 따른 이용자의 권리는 위의 내용에 의하여 영향을 받지 않습니다.

이것은 [이용허락규약\(Legal Code\)](#)을 이해하기 쉽게 요약한 것입니다.

[Disclaimer](#)

공학박사학위논문

Development of cube-on-face  
texture induced by surface  
nucleation in Fe-Si electrical steel

Fe-Si 전기강판 재료의 표면핵생성 유도에 의한  
cube-on-face 집합조직 형성에 관한 연구

2021년 2월

서울대학교 공과대학원  
재료공학부  
안 용 근

# Development of cube-on-face texture induced by surface nucleation in Fe-Si electrical steel

지도교수 황 농 문

이 논문을 공학박사학위논문으로 제출함

2020년 12월

서울대학교 대학원  
재료공학부

안 용 근

안용근의 박사학위논문을 인준함  
2020년 12월

위 원 장  
부위원장  
위 원  
위 원  
위 원

한 흥 남  
황 농 문  
박 은 수  
한 찬 희  
박 형 기



# Abstract

## Development of cube-on-face texture induced by surface nucleation in Fe-Si electrical steel

Yong-Keun Ahn

Department of Materials Science and Engineering

The Graduate School

Seoul National University

Electrical steel can be divided into Grain-Oriented electrical steel [GO] and Non-Oriented electrical steel [NO]. In the case of the GO, it is used as a material for transformers. Magnetic properties for the GO can be enhanced by a Goss texture development that forms a specific orientation of  $\{110\}\langle 001\rangle$ . On the other hand, the NO is used as a material for rotating motors and generators. Normally, magnetic properties of electrical steel can be controlled by a composition, microstructure, and texture development of the material. Until now, in the case of the NO, efforts are focused on the optimizing properties by controlling the composition of materials. Cube-on-face texture is ideal for NO, and has an orientation of  $\{100\}\langle 0vw\rangle$ , it performs excellent

magnetic properties in the direction of rotation. However, only a few studies on the texture development to enhance a magnetic property have been progressed.

In this study, it was confirmed that the texture development was changed by a stress applied to the specimen during  $\gamma \rightarrow \alpha$  phase transformation. Especially, a strong cube-on-face texture can be developed when the specimen is physically contacted with dissimilar materials which have difference in thermal expansion coefficient between the specimen and contacted materials during  $\gamma \rightarrow \alpha$  phase transformation. From these results, our group hypothesize that the nucleation barrier of the  $\alpha$  generated on the specimen surface was lowered due to the difference in the thermal expansion coefficient during  $\gamma \rightarrow \alpha$  phase transformation, and that of the orientation of  $\alpha$  would form  $\{100\} \langle 0vw \rangle$ . Thus, the hypothesis indicate that the surface nucleation is a key factor in the formation of a cube-on-face texture.

In order to use the stress effect applied to the specimen, applying tension to the specimen by creep deformation during  $\gamma \rightarrow \alpha$  phase transformation using the self-load was devised. A strong cube-on-face texture was developed using this method in Fe-2wt%Si-1wt%Ni. In addition, a batch process was considered to increase the possibility of applying to the industrial process. The

specimen was placed as upright position which is under the compressive stress during  $\gamma \rightarrow \alpha$  phase transformation. Using this method, a strong cube-on-face texture was developed.

In electrical steel, as the Si composition increases, the resistivity increase, which leads to reduce the core loss. Therefore, increasing resistivity by an adding Si content is essential. However, as the Si content increases, the material becomes brittle which couldn't progress a rolling process. Therefore, about 3wt%Si of electrical steel is produced in the industrial process. In order to enhance the advantageous of Si content and reduce the disadvantageous of the workability, a new concept was devised using Si diffusion to develop a cube-on-face texture. 10.69wt%Si composition and 81.9% of  $\{100\} \langle 0vw \rangle$  texture was developed using diffusion method, and a strong cube-on-face texture with a maximum of 96.8% was successfully developed.

**Keyword** : Fe-Si electrical steel; Phase transformation; Surface nucleation; Cube-on-face texture; Magnetic property

**Student Number** : 2018-34848

# Table of Contents

Chapter 1. Introduction.....	11
1.1 Electrical steel.....	11
1.2 Cube-on-face texture.....	16
Chapter 2. Fabrication of cube-on-face textured electrical steel using surface nucleation during $\gamma \rightarrow \alpha$ phase transformation .....	19
2.1 Introduction.....	19
2.2 Experimental procedure.....	21
2.3 Results & Discussion.....	26
Chapter 3. Uniaxial stress effect for the cube-on-face texture development during $\gamma \rightarrow \alpha$ phase transformation in Fe-2wt%Si-1wt%Ni electrical steel.....	41
3.1 Experimental procedure.....	41
3.2 Uniaxial stress effect for the development of cube-on-face texture..	45
3.3 Magnetic properties by a texture development.....	56
Chapter 4. Texture evolution of non-oriented electrical steel	

analyzed by EBSD and in-situ XRD during the phase transformation from $\gamma$ to $\alpha$ .....	60
4.1 Experimental procedure.....	60
4.2 Results & Discussion.....	63
Chapter 5. A new method for the evolution of strong cube-on-face texture induced by $\gamma \rightarrow \alpha$ phase transformation with the silicon diffusion in Fe-Si electrical steel .....	78
5.1 Introduction.....	78
5.2 Experimental procedure.....	79
5.3 Diffusion induced by B-doped Si wafer.....	85
5.4 Diffusion induced by Si powder.....	113
Chapter 6. Conclusions .....	119
Abstract in Korean .....	125



## List of Figures

Fig. 1.1 schematics of energy loss separation as a function of frequency.

Fig. 1.2 Resistivity change according to alloy contents.

Fig. 1.3 Magnetization curves along the various crystallographic directions.

Fig. 2.1 Schematics showing how the specimen is placed during the heat treatment. (a) The specimen is not in physical contact with the holding plate but (b) both sides of the specimen are in physical contact with  $\text{Al}_2\text{O}_3$ , quartz, tungsten or nickel plates.

Fig. 2.2 Schematics showing how the specimen is placed during the heat treatment. (a) The specimen is suspended with its front and rear ends paced on the quartz frame before the heat treatment. (b) The specimen is plastically deformed after the heat treatment under the condition of (a).

Fig. 2.3 EBSD IPF ND maps of the surface of Fe-1wt%Si annealed at 1100 °C for 5 min in  $\text{H}_2$  for the specimens (a) not in contact, (b)

in contact with the  $\text{Al}_2\text{O}_3$  plate. (d) and (e) are ODFs at  $\varphi_2 = 45^\circ$  section for (a) and (b), respectively.

Fig. 2.4 EBSD IPF ND maps of the surface of Fe-1wt%Si annealed at 1100 °C for 5 min in  $\text{H}_2$  for the specimens (a) in contact with the quartz plate, (b) in contact with the tungsten, and (c) in contact with the nickel plate. (d), (e) and (f) are ODFs at  $\varphi_2 = 45^\circ$  section for (a), (b) and (c), respectively.

Fig. 2.5 EBSD IPF ND maps of the specimen annealed at 1100 °C for 5 min in  $\text{H}_2$  for (a) Fe-1wt%Si and (b) Fe-2wt%Si-1wt%Ni. (c) and (d) are ODFs at  $\varphi_2 = 45^\circ$  section for (a) and (b), respectively.

Fig. 2.6 Schematics of the cross section of the plate specimen comparing the number of sites for triple junctions on the surface with that for quadruple points in the bulk for (a) small grain size and (b) large grain size.

Fig. 2.7 EBSD IPF ND maps of the surface of Fe-2wt%Si-1wt%Ni after annealing at 1100 °C in  $\text{H}_2$  for (a) 2 h, (b), 12 h and (c) 24 h. (d), (e) and (f) are ODFs at  $\varphi_2 = 45^\circ$  section for (a), (b) and (c),

respectively.

Fig. 2.8 Plots of the average  $\alpha$  grain size in IPF maps and percentages of  $\{100\}$  and  $\{111\}$  for Fe-2wt%Si-1wt%Ni against the heat treatment time.

Fig. 3.1 Schematic images of heat treatment conditions: (a) shows that the specimen is placed under recumbent position on the Ni plate. (b) shows that the specimen is placed under upright position.

Fig. 3.2 EBSD inverse pole figure ND maps of Fe-2wt%Si-1wt%Ni specimens were placed under the recumbent position on the nickel plate annealed at 1100 °C in H<sub>2</sub> for (a) 1 min, (b), 15 min and (c) 60 min. (d), (e) and (f) are ODFs at  $\varphi_2 = 45^\circ$  section for (a), (b) and (c), respectively.

Fig. 3.3 EBSD inverse pole figure ND maps of Fe-2wt%Si-1wt%Ni specimens were placed under the upright position annealed at 1100 °C in H<sub>2</sub> for (a) 1 min, (b), 15 min and (c) 60 min. (d), (e) and (f) are ODFs at  $\varphi_2 = 45^\circ$  section for (a), (b) and (c), respectively.

Fig. 3.4 plot of the average  $\alpha$  grain size against the annealing time

under different specimen placement.

Fig. 3.5 plot of  $\{100\}$  and  $\{111\}$  texture development against the annealing time under different specimen placement.

Fig. 3.6 EBSD inverse pole figure ND maps of Fe-2wt%Si-1wt%Ni specimens annealed at 1100 °C for 60min in H<sub>2</sub>: (a) the specimen was placed under the recumbent position on the nickel plate, (b) the specimen was placed under the upright position. (c) and (d) are ODFs at  $\varphi_2 = 45^\circ$  section for (a) and (b), respectively.

Fig. 3.7 EBSD inverse pole figure ND maps of Fe-2wt%Si-1wt%Ni specimen to confirm the relationship between magnetic properties and the (100) texture development. (a) 78.4% of (100), (b) 35.6% of (100) and (c) 0.7% of (100). (d), (e) and (f) are ODFs at  $\varphi_2 = 45^\circ$  section for (a), (b) and (c), respectively.

Fig. 3.8 Plots for the magnetic properties of specimens with controlled texture and commercial non-oriented electrical steel.

Fig. 4.1 EBSD inverse pole figure ND maps of (a) Fe-2wt%Si-1wt%Ni and (b) Fe-3wt%Si-2.5wt%Ni and  $45^\circ$  sections of ODF of

(c) Fe-2wt%Si-1wt%Ni and (d) Fe-3wt%Si-2.5wt%Ni after the specimens were annealed at 1100 °C for 4 h under flowing H<sub>2</sub>.

Fig. 4.2 In-situ XRD peaks of Fe-2%Si-1%Ni during heating from 400 °C to 1200 °C.

Fig. 4.3 In-situ XRD peaks of Fe-2%Si-1%Ni during cooling from 1200 °C to 400 °C.

Fig. 4.4 In-situ XRD peaks of Fe-3%Si-2.5%Ni during heating from 400 °C to 1200 °C.

Fig. 4.5 In-situ XRD peaks of Fe-3%Si-2.5%Ni during cooling from 1200 °C to 400 °C.

Fig. 4.6 Comparison of the XRD peak intensity during cooling of the specimens with those of the powder of the same composition (a) for Fe-3wt%Si-2.5wt%Ni and (b) for Fe-2wt%Si-1wt%Ni.

Fig. 5.1 DSC profile of the Fe-1wt%Si specimen measured during heating.

Fig. 5.2 Annealing condition for the  $\gamma \rightarrow \alpha$  phase transformation with commercially pure Si powder.

Fig. 5.3 Schematic image of heat treatment condition to enhance the bonding pressure.

Fig. 5.4 Schematic of before & after Si diffusion image for Fe-1wt%Si specimen with B-doped Si wafer.

Fig. 5.5 Photo image of before & after Si diffusion for Fe-1wt%Si specimen with B-doped Si wafer.

Fig. 5.6 EBSD IPF ND maps and  $45^\circ$  sections of ODF for the surface of specimens in Fe-1wt%Si annealed for 5 min with  $H_2$  gas: (a), (c) at 1100 °C without contact and (b), (d) at 1100 °C in contacting with B-doped Si wafer.

Fig. 5.7 EBSD IPF ND maps and  $45^\circ$  sections of ODF for the surface of specimens in Fe-1wt%Si annealed for 5 min with  $H_2$  gas: (a), (c) at 1050 °C in contacting with B-doped Si wafer and (b), (d) at 1000 °C in contacting with B-doped Si wafer.

Fig. 5.8 Si diffused specimens according to increase holding time at 1100 °C : (a) 2 min, (b) 3.75 min, (c) 7.5 min, (d) 15 min (e) 30 min and (f) 60 min.

Fig. 5.9 EBSD IPF ND maps and 45° sections of ODF for the surface of Si diffused specimens according to increase holding time at 1100 °C in Fe-1wt%Si contact with B-doped Si wafer: (a), (d) 2 min (b), (e) 3.75 min and (d), (f) 7.5 min.

Fig. 5.10 EBSD IPF ND maps and 45° sections of ODF for the surface of Si diffused specimens according to increase holding time at 1100 °C in Fe-1wt%Si contact with B-doped Si wafer: (a), (d) 15 min (b), (e) 30 min and (d), (f) 60 min.

Fig. 5.11 Grain size distribution for Si diffused specimens with increased diffusion time at 1100 °C.

Fig. 5.12 Percentages of major orientations for Si diffused specimens with increased diffusion time at 1100 °C.

Fig. 5.13 EBSD IPF ND maps for the cross section of Si diffused specimens according to increase holding time at 1100 °C in Fe-

1wt%Si contact with B-doped Si wafer: (a) 2 min, (b) 3.75 min sec and (c) 7.5 min, respectively.

Fig. 5.14 EBSD IPF ND maps for the cross section of Si diffused specimens according to increase holding time at 1100 °C in Fe-1wt%Si contact with B-doped Si wafer: (a) 15 min, (b) 30 min sec and (c) 60 min, respectively.

Fig. 5.15 Line EDS images for the cross section of Si diffused specimens according to increase holding time at 1100 °C in Fe-1wt%Si contact with B-doped Si wafer: (a) 2 min, (b) 3.75 min and (c) 7.5 min, respectively.

Fig. 5.16 Line EDS images for the cross section of Si diffused specimens according to increase holding time at 1100 °C in Fe-1wt%Si contact with B-doped Si wafer: (a) 15 min, (b) 30 min and (c) 60 min, respectively.

Fig. 5.17 EDS mapping images of the upper side area of the specimen after Si diffusion: (a) Fe-Si layer, (b) Fe<sub>2</sub>-Si and (c) Ferrite, respectively.



Fig. 5.18 Schematic of the cross sectional image after completion of Si diffusion.

Fig. 5.19 EDS mapping images of the upper side area of the specimen according to increase holding time at 1100 °C in Fe-1wt%Si contact with B-doped Si wafer: (a) 2 min, (b) 3.75 min and (c) 7.5 min, respectively.

Fig. 5.20 EDS mapping images of the upper side area of the specimen according to increase holding time at 1100 °C in Fe-1wt%Si contact with B-doped Si wafer: (a) 15 min, (b) 30 min and (c) 60 min, respectively.

Fig. 5.21 Schematics of alloying layers and voids formation during Si diffusion process.

Fig. 5.22 EBSD IPF ND maps and 45° sections of ODF for the surface of Si diffused specimens at 1100 °C holding for 5 min in Fe-1wt%Si contact with Si powders: (a) IPF map and (b) ODF.

Fig. 5.23 EBSD IPF ND maps and 45° sections of ODF for the surface of Si diffused specimens at 1100 °C holding for 12 h in Fe-

1wt%Si contact with Si powders: (a) IPF map and (b) ODF.

Fig. 5.24 SEM cross sectional image at 1100 °C holding for 5 min in Fe-1wt%Si pressed by Al<sub>2</sub>O<sub>3</sub> plate.

Fig. 5.25 EBSD IPF ND maps for the cross section of Si diffused specimens at 1100 °C in Fe-1wt%Si pressed by a Al<sub>2</sub>O<sub>3</sub> plate.

# Chapter 1. Introduction

## 1.1. Electrical steel

Electrical steel can be divided into two fields. When the direction of magnetic property in the core is fixed, grain-oriented electrical steel [GO] is used [1–5]. In the case where the position of motors and generators is not fixed, however, non-oriented electrical steel [NO] is used [6–12]. Recent years, eco-friendly technology such as electrical vehicles and wind powers is becoming popular increasingly. Especially, electrical vehicles are expected to replace a large portion of the vehicles using internal combustion engine, which expect would be extended to the need of high efficiency electrical engine [13–15]. It is well known that a cube-on-face texture of  $\{100\} \langle 0vw \rangle$  is ideal for non-oriented electrical steel because the cube-on-face texture has excellent magnetic properties in motors and generations [16–26].

Fig. 1.1 shows a total energy loss in electrical steel. The total loss ( $W_{\text{total}}$ ) is sum of  $W_h$ ,  $W_{ec}$  and  $W_{ea}$ .  $W_h$  mean the hysteresis loss,  $W_{ec}$  means eddy current loss, and  $W_{ea}$  means anomalous loss. In the case of the eddy current loss ( $W_{ec}$ ),  $d$  is sheet thickness,  $I$  is magnetic induction,  $f$  is frequency  $\rho$  is resistivity, and  $2L$  is domain size. Therefore, magnetic properties for the electrical steel can be

enhanced by adding components which could enhance the resistivity. Especially, the resistivity is closely related to the energy loss as shown in Fig. 1.2 which shows the resistivity against the composition. As the Si content increases the resistivity increases and the resistivity increases  $W_{ec}$  decreases, which leads to reduce the core loss. Fig. 1.3 shows the change in the degree of magnetization in the electrical steel material depending on the crystal orientation. When a magnetic field is applied, the magnetization occurs in all crystal directions. When the magnetic field is sufficiently large, the electrical steel becomes saturated and no further magnetization occurs even if the magnetic field is increased. Normally, electrical steels are used under conditions of low saturation magnetization. In this case, it can be seen that the  $\langle 100 \rangle$  crystal direction is the most easily magnetized, the  $\langle 110 \rangle$  crystal direction is the second easily magnetized, and the  $\langle 111 \rangle$  crystal direction is the most difficult to magnetize. Therefore, if the  $\langle 100 \rangle$  direction coincides with the direction to be used, the material can exhibit the best properties because lower energy required for magnetization is consumed.

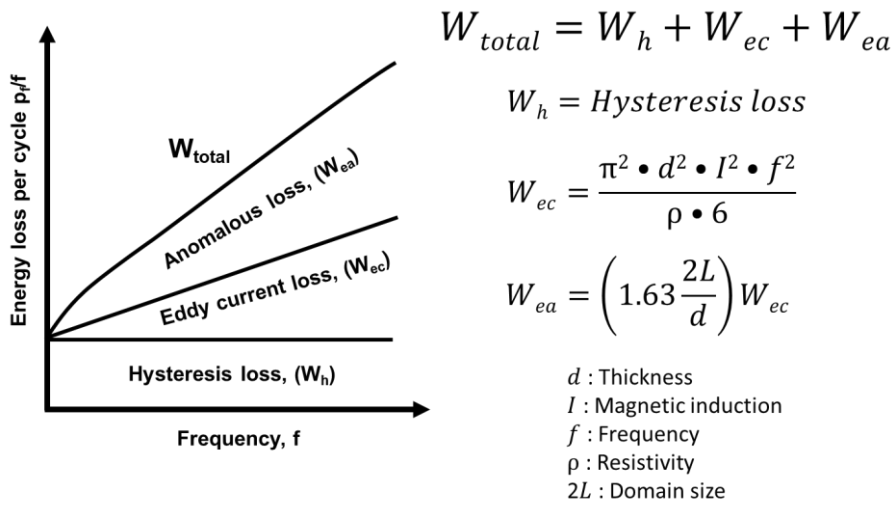


Fig. 1.1 schematics of energy loss separation as a function of frequency.

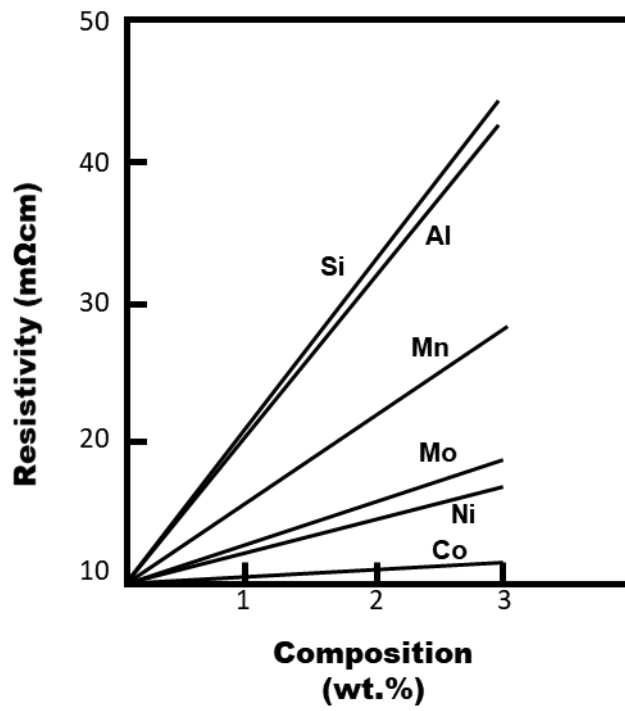


Fig. 1.2 Resistivity change according to alloy contents.

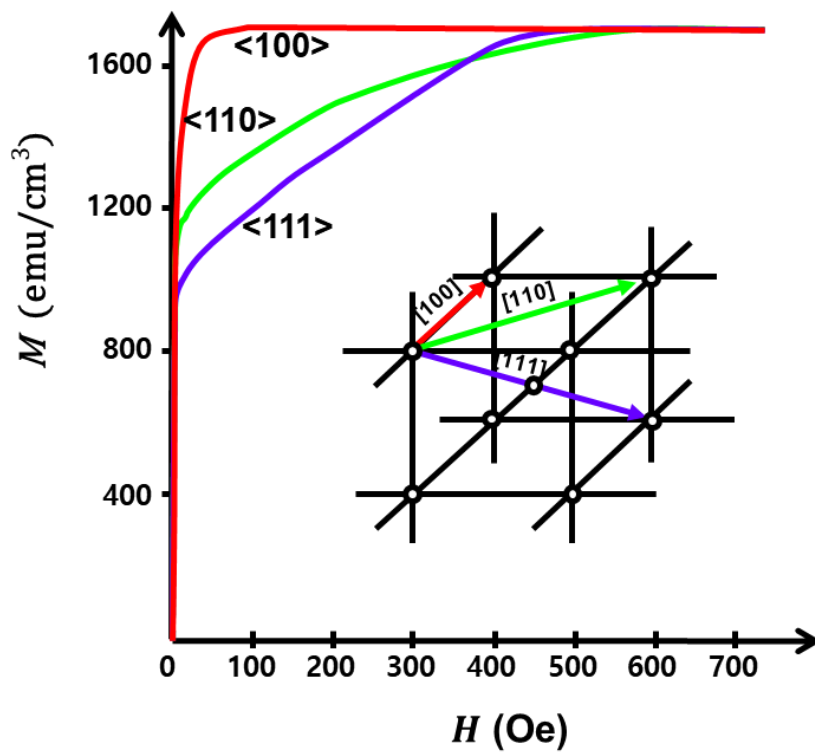


Fig. 1.3 Magnetization curves along the various crystallographic directions.

## 1.2. Cube-on-face texture

In recent years, as the demand for electrical vehicles has increased and the expectations for future growth have increased. Electrical vehicles are expected to replace a large portion of the vehicles using internal combustion engine, which expect would be extended to the need of high efficiency electrical engine [5, 14]. It is well known that the cube-on-face texture of  $\{100\}\langle 0vw \rangle$  is ideal for non-oriented electrical steel because each grain has two easy magnetization directions in the plane of the sheet which gives excellent magnetic properties and isotropic properties [8, 21, 27–29].

Tomida et al. [13, 28, 30, 31] developed a  $\{100\}\langle 0vw \rangle$  texture using two-stage annealing process, where the annealing process for phase transformation was conducted by removing manganese in vacuum atmosphere followed by the decarburization process to induce the inward growth. During the vacuum annealing process under higher than  $10^{-3}$  Pa in  $\gamma$  phase region or  $\alpha + \gamma$  dual phase region, manganese vaporization occurs, resulting in  $\gamma \rightarrow \alpha$  phase transformation. Nucleation seeds which nucleated by manganese vaporization have a  $\{100\}\langle 0vw \rangle$  orientation.

JK Sung et al. [8, 32] reported that a strong cube-on-face texture was developed using  $\alpha \rightarrow \gamma \rightarrow \alpha$  phase transformation in



pure hydrogen atmosphere. They suggested that formation of  $\{100\}\langle 0vw\rangle$  nucleus is related to the elastic anisotropy. The elastic strain energy of the nucleus with  $\{100\}\langle 0vw\rangle$  orientation is minimized on the specimen surface and oxygen partial pressure is major factor to reduce surface oxidization.

Kwon et al. [33] also reported the cube-on-face texture development using phase transformation. They found out that physicals contact with dissimilar materials could make a strong effect on the evolution of cube-on-face texture. The physical effect induced by difference in thermal expansion coefficient during  $\gamma \rightarrow \alpha$  phase transformation on the specimen surface reduce the nucleation barrier resulting in strong cube-on-face texture development.

On the other hand, Heo et al. [34] developed a  $\{100\}\langle 0vw\rangle$  texture without phase transformation using the surface energy anisotropy controlled by sulfur. The surface energy of  $\{110\}$  is lower than that of  $\{100\}$ , which is again lower than that of  $\{111\}$  in BCC Fe. When the BCC is annealed in the atmosphere containing sulfur, the surface energy of  $\{100\}$  becomes lower than that of  $\{110\}$ , producing a strong  $\{100\}\langle 0vw\rangle$  texture.

From previous results, our group hypothesized the development of cube-on-face texture. During  $\gamma \rightarrow \alpha$  phase transformation,  $\alpha$

phase nucleate in the  $\gamma$  phase matrix, which is under the compressive stress because the molar volume of BCC is larger than that of FCC. Since the strain energy is proportional to the Young's modulus or shear modulus, the resultant strain would increase the nucleation barrier. Therefore, if a specimen is under the 2D stress, nucleation barrier is minimum in the direction where the Young's modulus is minimum which leads to development of  $\{100\}\langle 0vw \rangle$  texture, because it is well known that the Young's modulus is minimum in the  $\langle 100 \rangle$  direction in Fe [32].

## **Chapter 2. Fabrication of cube-on-face textured electrical steel using surface nucleation during $\gamma \rightarrow \alpha$ phase transformation**

### **2.1. Introduction**

When any specimen undergoes heat treated, it should be placed on a supporting material, which is in physical contact with the specimen. So far, little attention has been paid to the possibility that such physical contact should have an effect on the texture evolution. However, we found out that such physical contact could affect the texture evolution of  $\{100\}\langle 0vw \rangle$  [35, 36]. In order to understand the effect of the physical contact, systematic experiments were performed using materials such as  $\text{Al}_2\text{O}_3$ , quartz, tungsten, and nickel for the physical contact with the specimen.

Since the result indicated that the tensile stress induced by the physical contact is responsible for the texture evolution of  $\{100\}\langle 0vw \rangle$ , a new method was devised to produce the texture of  $\{100\}\langle 0vw \rangle$  more easily. Here, a specimen was suspended horizontally with the front and rear ends of the specimen supported by a holder. Then, the center of the specimen undergoes the creep deformation by a self-load during the heat treatment, producing the tensile stress on the surface and thereby producing the texture of  $\{100\}\langle 0vw \rangle$ . In this chapter, it was studied how the tensile stress

induced by the physical contact and by the creep deformation due to the self-load during heat treatment affects the texture evolution of  $\{100\} \langle 0vw \rangle$  in Fe-Si steel.

## 2.2. Experimental procedure

Fe-1wt%Si and Fe-2wt%Si-1wt%Ni ingots, prepared by vacuum induction melting, were hot rolled to 2.3 mm and cold rolled to 0.35 mm thickness. The composition of Fe-2wt%Si is outside of the  $\gamma$  loop in the Fe-Si phase diagram. Therefore, the texture control using  $\gamma \rightarrow \alpha$  transformation is not possible. This is why 1wt%Ni is added to Fe-2wt%Si so that the composition of Fe-2wt%Si-1wt%Ni may fall in the  $\gamma$  phase region at the heat treatment temperature.

Our previous experiments confirmed that the physical contact of the Fe-1wt%Si specimen with the supporting Al<sub>2</sub>O<sub>3</sub> plate increased the percentage of {100} <0vw> [33]. This chapter is the extension of this previous work to clarify which is responsible for the evolution of {100} <0vw>. To check whether the increase in the percentage of {100} <0vw> comes from the physical contact or not, the hollow rectangular frame was used as a specimen holder as shown in Fig. 2.1a. In order to study the effect of the physical contact with various materials such as Al<sub>2</sub>O<sub>3</sub>, quartz, tungsten and nickel plates, the specimen was sandwiched between these plates as shown in Fig. 2.1b. The specimen size of Fig. 2.1a and b was 15 mm × 30 mm × 0.35 mm whereas the size of Al<sub>2</sub>O<sub>3</sub>, quartz, tungsten

and nickel plates was 20 mm × 30 mm × 0.6 mm, so that the plates could cover the whole specimen. Specimens were heated to 1100 °C of the  $\gamma$  phase region at 10 °C/min, held for 5 min, cooled to 950 °C for 2 h and cooled to room temperature in the furnace under flowing H<sub>2</sub>. During cooling, the specimen underwent  $\gamma \rightarrow \alpha$  phase transformation.

In order to study the effect of the tension of the specimen surface arising from the plastic deformation or the creep of the specimen by its own weight during heat treatment, the specimen was suspended on the quartz frame as shown in Fig. 2.2a. During the heat treatment, however, it underwent creep, being plastically deformed by the self-load as shown in Fig. 2.2b. The Fe-1wt%Si specimen was heated to 1100 °C of the  $\gamma$  phase region at 10 °C/min, held for 5 min, cooled to 950 °C for 2 h and cooled to room temperature in the furnace.

Since the highest percentage of the  $\{100\}\langle 0vw \rangle$  was obtained for the Fe-1wt%Si specimen in the condition of Fig. 2.2, more systematic experiments were performed in this condition for the Fe-2wt%Si-1wt% Ni specimen, which was held at 1100 °C of the  $\gamma$  phase region for 5 min, 2 h, 12 h and 24 h to vary the grain size with the other experimental conditions being the same as those of Fe-1wt%Si.

To investigate the texture evolution after the heat treatment, the specimen surface was polished to a final stage of colloidal silica (OP-s, 0.04  $\mu\text{m}$ ) and analyzed by electron back-scattered diffraction (EBSD, EDAX/Hikari) attached to a field emission scanning electron microscope (FESEM, SU5000, HITACHI). The EDAX/TSL software was used to analyze the orientation relationship.

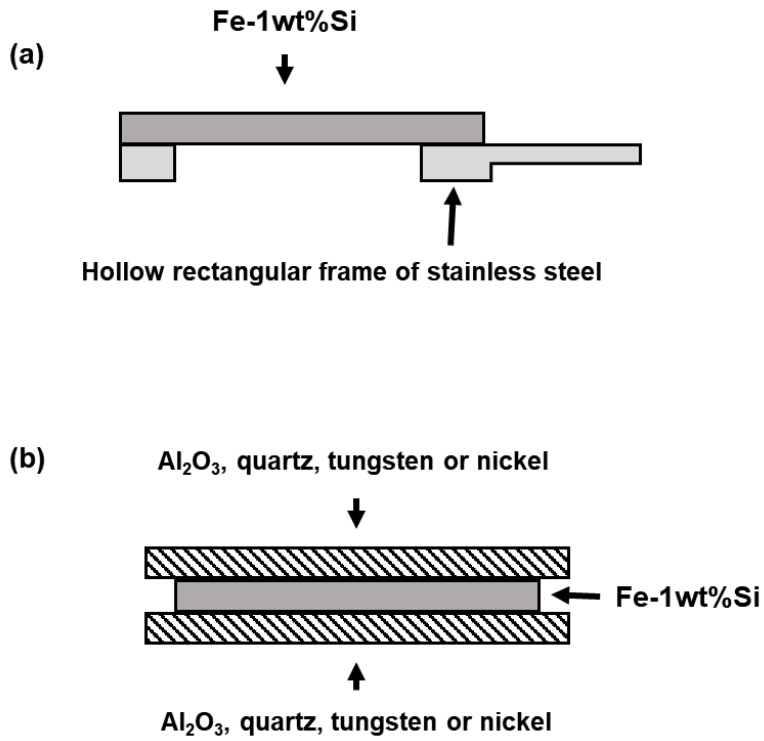


Fig. 2.1 Schematics showing how the specimen is placed during the heat treatment. (a) The specimen is not in physical contact with the holding plate but (b) both sides of the specimen are in physical contact with Al<sub>2</sub>O<sub>3</sub>, quartz, tungsten or nickel plates.



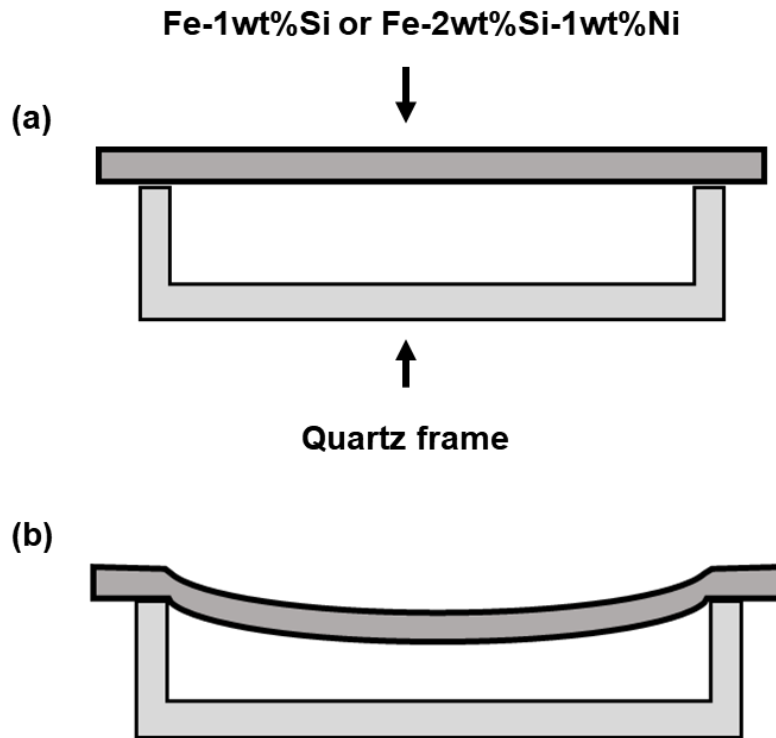


Fig. 2.2 Schematics showing how the specimen is placed during the heat treatment. (a) The specimen is suspended with its front and rear ends paced on the quartz frame before the heat treatment. (b) The specimen is plastically deformed after the heat treatment under the condition of (a).

### 2.3. Results & Discussions

Fig. 2.3a and c shows the inverse pole figure (IPF) map and the orientation distribution function (ODF) sectioned at  $\varphi_2 = 45^\circ$ , respectively, for the Fe-1wt%Si specimen heat treated under the condition of Fig. 2.1a. Percentages of  $\{100\}\langle 0vw \rangle$  and  $\{111\}\langle uvw \rangle$  were 14.3% and 22.4%, respectively, which were determined using the criteria of  $\{hkl\} \pm 15^\circ$ .

Fig. 2.3b and d shows the IPF map and the ODF, respectively, for Fe-1wt%Si heat treated under the condition of Fig. 2.1b, where the specimen was in contact with both sides of the  $Al_2O_3$  plate. Percentages of  $\{100\}\langle 0vw \rangle$  and  $\{111\}\langle uvw \rangle$  were 76.3% and 10.5%, respectively. The average grain sizes of Fig. 2.3a and b were 232  $\mu m$  and 196  $\mu m$ , respectively, which were determined by converting the grain area into the diameter using an image analyzer software (EDAX/TSL software).

Fig. 2.3a and b shows that the percentage of  $\{100\}\langle 0vw \rangle$  strongly depends on the presence and the absence of the physical contact with the  $Al_2O_3$  plate. The possible effect of the physical contact would be the surface stress caused by the friction between the specimen and its holder, arising from the difference in the thermal expansion coefficient. The thermal expansion coefficient of

Fe is  $11.8 \times 10^{-6} \text{ }^\circ\text{C}^{-1}$  and those of  $\text{Al}_2\text{O}_3$ , quartz, tungsten, and nickel are respectively 5.4, 0.55, 3.7, and  $13.3 \times 10^{-6} \text{ }^\circ\text{C}^{-1}$  [37–39]. It should be noted that thermal expansion coefficients of  $\text{Al}_2\text{O}_3$ , quartz and tungsten are less than a half of that of Fe whereas Ni has a value similar to that of Fe. To check the possibility that the difference in the thermal expansion coefficient between the specimen and its holder is related with the evolution of  $\{100\}\langle 0vw\rangle$ , the experiment similar to Fig. 2.3b was performed using quartz, tungsten, and nickel plates.

Fig. 2.4a and d shows the IPF map and the ODF, respectively, for Fe–1wt%Si heat treated under the condition of Fig. 2.1b, where the specimen was in contact with both sides of the quartz plate. Percentages of  $\{100\}\langle 0vw\rangle$  and  $\{111\}\langle uvw\rangle$  were 76.4% and 10.4%, respectively. Fig. 2.4b and e shows the IPF map and the ODF, respectively, for the specimen heat treated under the condition of Fig. 2.1b, where the specimen was in contact with both sides of the tungsten plate. The percentages of  $\{100\}\langle 0vw\rangle$  and  $\{111\}\langle uvw\rangle$  were 74.7% and 11.7%, respectively. Fig. 2.4c and f shows the IPF map and the ODF, respectively, for Fe–1wt%Si heat treated under the condition of Fig. 2.1b, where the specimen was in contact with both sides of the nickel plate. Percentages of  $\{100\}\langle 0vw\rangle$  and  $\{111\}\langle uvw\rangle$  were 17.8% and 54.1%, respectively.

The average grain sizes of Fig. 2.4a, b, and c were 213  $\mu\text{m}$ , 204  $\mu\text{m}$ , and 146  $\mu\text{m}$ , respectively.

Fig. 2.3b, Fig. 2.4a and b show that the physical contact of the Fe-1wt%Si specimen with  $\text{Al}_2\text{O}_3$ , quartz, and tungsten plates produced a high percentage of  $\{100\}\langle 0vw\rangle$  whereas the physical contact with nickel in Fig. 2.4c produced a low percentage of  $\{100\}\langle 0vw\rangle$ . Therefore, the evolution of  $\{100\}\langle 0vw\rangle$  has a strong correlation with the thermal expansion coefficient of the specimen holder in physical contact. One possible explanation would be as follows. During the cooling process, Fe-1wt%Si with a higher thermal expansion coefficient would shrink more than  $\text{Al}_2\text{O}_3$ , quartz, and tungsten, which would generate the friction between the two materials. This friction would be proportional to the difference in the thermal expansion coefficient. Therefore, for  $\text{Al}_2\text{O}_3$ , quartz, and tungsten, the friction or the tensile stress on the specimen surface would be relatively large but for nickel, it would be relatively small or negligible. This difference seems to be responsible for the difference in the texture evolution.

$\alpha$  BCC and  $\gamma$  FCC, which are densities of BCC and FCC Fe, are 7.86  $\text{g}/\text{cm}^3$  and 8.60  $\text{g}/\text{cm}^3$ , respectively, and the molar volume of BCC Fe is larger than that of FCC Fe. Therefore, when BCC  $\alpha$  nucleates from FCC  $\gamma$ , the nucleus would be under the compressive

stress. The resultant strain energy would increase the nucleation barrier. Since the strain energy is proportional to the Young's modulus or the shear modulus, the nucleation barrier would be minimum in the direction where the Young's modulus is minimum. It is known that the Young's modulus is minimum in the  $\langle 100 \rangle$  direction in Fe [32]. Therefore, if the  $\{100\} \langle 0vw \rangle$  nucleus is formed on the surface, the nucleus would have the minimum nucleation barrier. Again if the  $\{100\} \langle 0vw \rangle$  nuclei formed on the surface grow dominantly into the bulk, the dominant  $\{100\} \langle 0vw \rangle$  texture would be evolved.

Under this situation, if the compressive stress is relieved by the tensile friction made by the physical contact, the nucleation barrier would be reduced and the nucleation of  $\{100\} \langle 0vw \rangle$  on the surface would be favored. This would be why the percentage of  $\{100\} \langle 0vw \rangle$  in Fig. 2.3b is much higher than that in Fig. 2.3a. In the case of  $\text{Al}_2\text{O}_3$ , quartz, and tungsten, the tensile frictional stress is appreciable and favors the nucleation of  $\{100\} \langle 0vw \rangle$  on the surface. It should be reminded that it took 2 h for cooling from 1100 °C to 950 °C with the cooling rate being rather low. At such a low cooling rate, the driving force for the nucleation of  $\alpha$  would be low. As a result, the nucleation rate would be low. Under this condition, once the nuclei of  $\{100\} \langle 0vw \rangle$  is formed, they would continue to grow

from the surface to the interior. As a result, the percentage of  $\{100\}\langle 0vw \rangle$  would be high and the grain size would be large as shown in Fig. 2.3b, Fig. 2.4a and b.

By a similar logic, the low percentage of  $\{100\}\langle 0vw \rangle$  and the small grain size in Fig. 2.4c can be explained. When the tensile frictional stress is small or negligible as in the case of the nickel plate, the nucleation of  $\{100\}\langle 0vw \rangle$  would not be favored and seemed not to take place on the surface during cooling from 1100 °C to 950 °C. The nucleation of other orientations would occur after the specimen was cooled relatively rapidly from 950 °C because the power of the furnace was off for further cooling, which would result in a high nucleation rate. As a result, the percentage of  $\{100\}\langle 0vw \rangle$  is low and the grain size is small as shown in Fig. 2.4c.

If the explanation on the effect of the physical contact is correct, the nucleation of  $\{100\}\langle 0vw \rangle$  on the surface can be favored by providing the surface stress in a way other than the physical contact. One possible way would be the tensile stress generated when the specimen was suspended as shown in Fig. 2.2a, which would undergo the high temperature creep or the plastic deformation triggered by the self-load during heat treatment as shown in Fig. 2.2b.

Fig. 2.5a and c shows the IPF map and the ODF, respectively,

for Fe-1wt%Si, which was heat treated under the condition of Fig. 2.2. The percentage of  $\{100\}\langle 0vw \rangle$  is 88.0%, which is the highest percentage in all specimens tested in this experiment. The surface stress of the specimen in Fig. 2.2b would be tensile on both sides because the specimen was elongated by the plastic deformation. This tensile stress appears to be effective in inducing the nucleation of the  $\{100\}\langle 0vw \rangle$  on the surface during  $\gamma \rightarrow \alpha$  transformation. This means that the self-load of the specimen has the effect similar to that of its physical contact with  $\text{Al}_2\text{O}_3$ , quartz and tungsten plates.

To check if this concept can be applied to the commercially-applicable silicon steel, a similar experiment was performed using the Fe-2wt%Si-1wt%Ni specimen, which has a higher silicon content than Fe-1wt%Si. Fig. 2.5b and d shows the IPF map and the ODF, respectively, for Fe-2wt%Si-1wt%Ni heat treated under the condition of Fig. 2.2, where the specimen was held at 1100 °C of the  $\gamma$  phase region for 5 min. Although we expected a high percentage of  $\{100\}\langle 0vw \rangle$ , the percentage of  $\{100\}\langle 0vw \rangle$  was only 1.8%. Instead,  $\{111\}\langle uvw \rangle$  was a major texture with its percentage of 77.7%.

One possibility for the result of Fe-2wt%Si-1wt%Ni specimen would be the small average grain size as shown in Fig. 2.5b, where the average grain size of  $\alpha$  is 105  $\mu\text{m}$  in contrast with 249  $\mu\text{m}$  for

the Fe-1wt%Si specimen in Fig. 2.5a. Here, the heat treatment condition was the same but the composition of the specimen was different. This composition difference would result in the different grain size. Therefore, the additional content of Si and Ni in the Fe-2wt%Si-1wt%Ni specimen seemed to decrease the average grain size by the solute drag effect [40], resulting in the small average grain size of  $\alpha$  in Fig. 2.5b in contrast with that in Fig. 2.5a.

Fig. 2.6 shows schematics explaining how the grain size can affect the evolution of  $\{100\}\langle 0vw \rangle$ . The site of the lowest nucleation barrier on the surface would be the triple junctions where the three grains meet, which are indicated as red circle dots. The site of the lowest nucleation barrier in the bulk would be the four grain corners, which are also indicated as blue square dots. If the grain size is large in the  $\gamma$  phase, the number of four grain corners in the bulk would decrease. Therefore, the nucleation of  $\alpha$  on the triple junction on the surface can be made dominant if the number of four grain corners is small or the grain size is large. If the grain size is small, however, the number of four grain corners would be large compared to the number of triple junctions on the surface. Then, the nucleation on four grain corners in the bulk can be dominant. Since the nucleation of  $\{100\}\langle 0vw \rangle$  is not favorable in the bulk, the percentage of  $\{100\}\langle 0vw \rangle$  would be low.



Since the increase in the  $\gamma$  grain size decreases the number of four grain corners, which would have the lowest nucleation barrier in the bulk, it would decrease the number of nucleation sites in the bulk. Then, it would provide the condition favorable for the growth of the grains of  $\{100\}\langle 0vw\rangle$ , which are expected to nucleate at the triple junction on the surface. To test this possibility, the effect of the holding time or the  $\gamma$  grain size on the percentage of  $\{100\}\langle 0vw\rangle$  grains was studied in the Fe-2wt%Si-1wt%Ni specimen. The Fe-2wt%Si-1wt%Ni specimens in Fig. 2.7a, b and c were held at 1100 °C for 2 h, 12 h and 24 h, respectively, which increased the average grain size from 105  $\mu\text{m}$  in Fig. 2.5b, respectively, to 119  $\mu\text{m}$ , 127  $\mu\text{m}$  and 235  $\mu\text{m}$ .

Fig. 2.7a, b and c shows the IPF maps with the corresponding ODFs shown by Fig. 2.7d, e and f. The percentages of  $\{100\}\langle 0vw\rangle$  in Fig. 2.7a, b and c were, respectively, 8.1%, 21.2% and 70.7% and the percentages of  $\{111\}\langle uvw\rangle$  were, respectively, 73.8%, 57.8% and 3.4% as determined from the IPF maps. These results show that the percentage of  $\{100\}\langle 0vw\rangle$  increased and the percentage of  $\{111\}\langle uvw\rangle$  decreased with increasing grain size.

This aspect is plotted in Fig. 2.8, where the average grain size of  $\alpha$  and the percentages of  $\{100\}\langle 0vw\rangle$  and  $\{111\}\langle uvw\rangle$  are plotted against the holding time. The dependence of the percentage

of  $\{100\}\langle 0vw \rangle$  on the holding time has a similar tendency as that of the average grain size whereas the percentage of  $\{111\}\langle uvw \rangle$  has a reversed tendency. These results indicate that the  $\{100\}\langle 0vw \rangle$  texture evolution increases with the grain size.

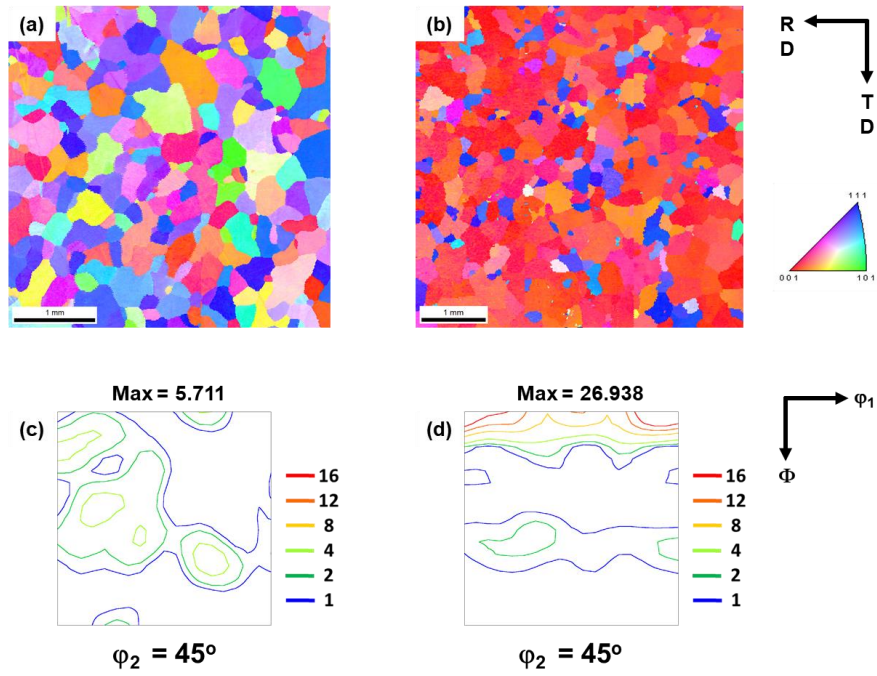


Fig. 2.3 EBSD IPF ND maps of the surface of Fe-1wt%Si annealed at 1100 °C for 5 min in H<sub>2</sub> for the specimens (a) not in contact, (b) in contact with the Al<sub>2</sub>O<sub>3</sub> plate. (d) and (e) are ODFs at  $\phi_2 = 45^\circ$  section for (a) and (b), respectively.

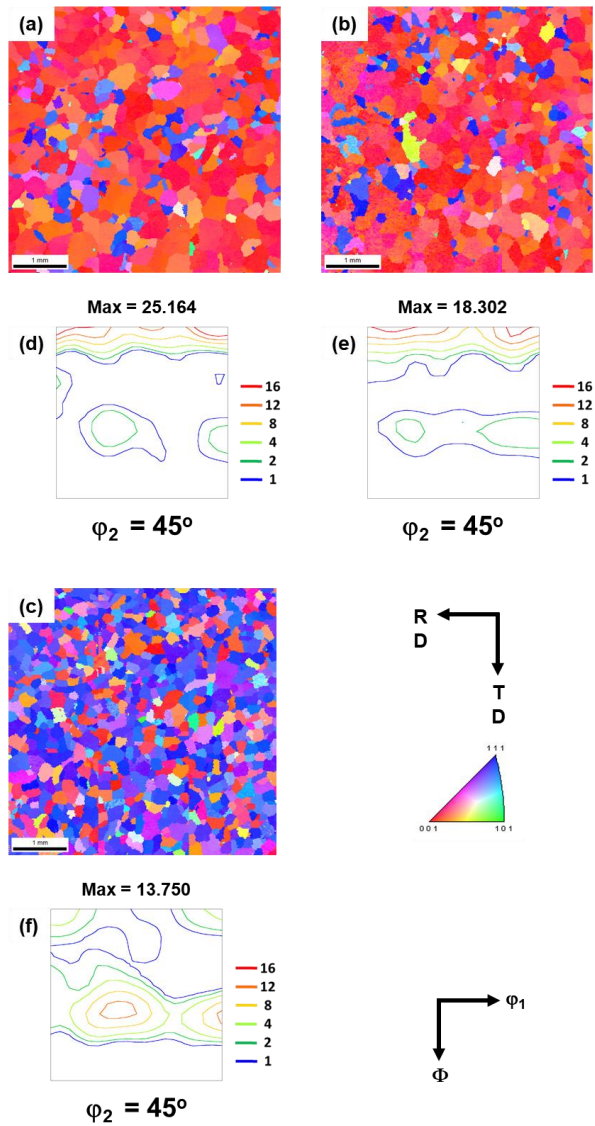


Fig. 2.4 EBSD IPF ND maps of the surface of Fe-1wt%Si annealed at 1100 °C for 5 min in H<sub>2</sub> for the specimens (a) in contact with the quartz plate, (b) in contact with the tungsten, and (c) in contact with the nickel plate. (d), (e) and (f) are ODFs at  $\varphi_2 = 45^\circ$  section for (a), (b) and (c), respectively.

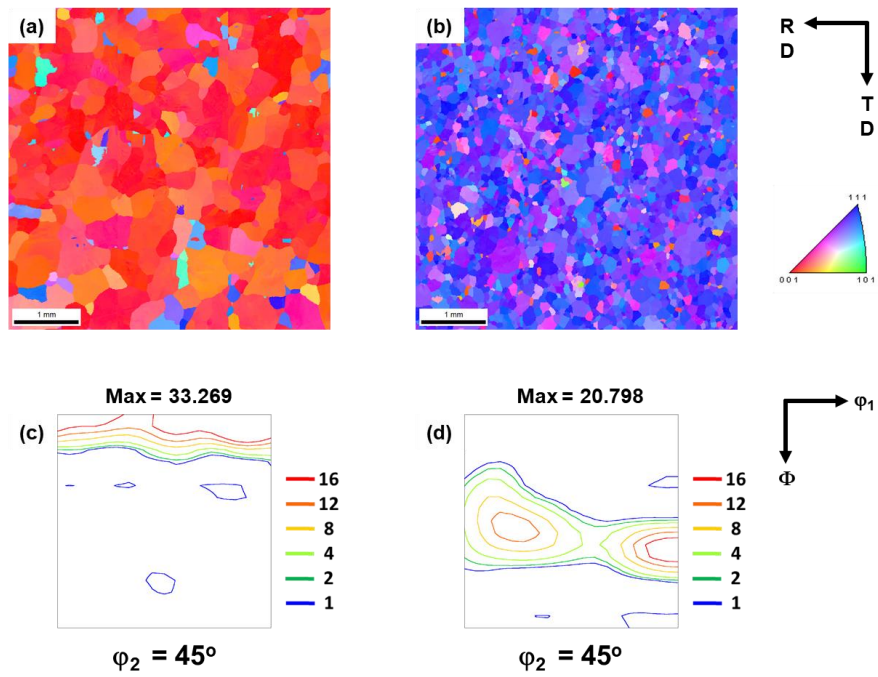


Fig. 2.5 EBSD IPF ND maps of the specimen annealed at 1100 °C for 5 min in H<sub>2</sub> for (a) Fe-1wt%Si and (b) Fe-2wt%Si-1wt%Ni. (c) and (d) are ODFs at  $\varphi_2 = 45^\circ$  section for (a) and (b), respectively.

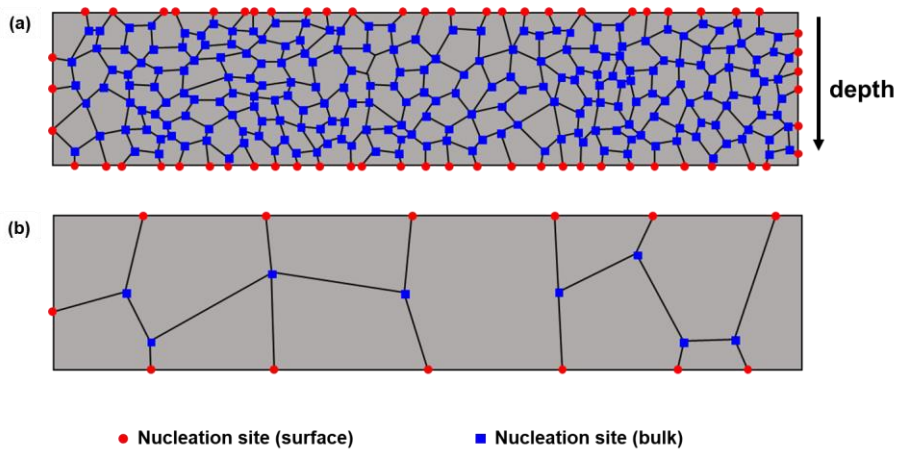


Fig. 2.6 Schematics of the cross section of the plate specimen comparing the number of sites for triple junctions on the surface with that for quadruple points in the bulk for (a) small grain size and (b) large grain size.

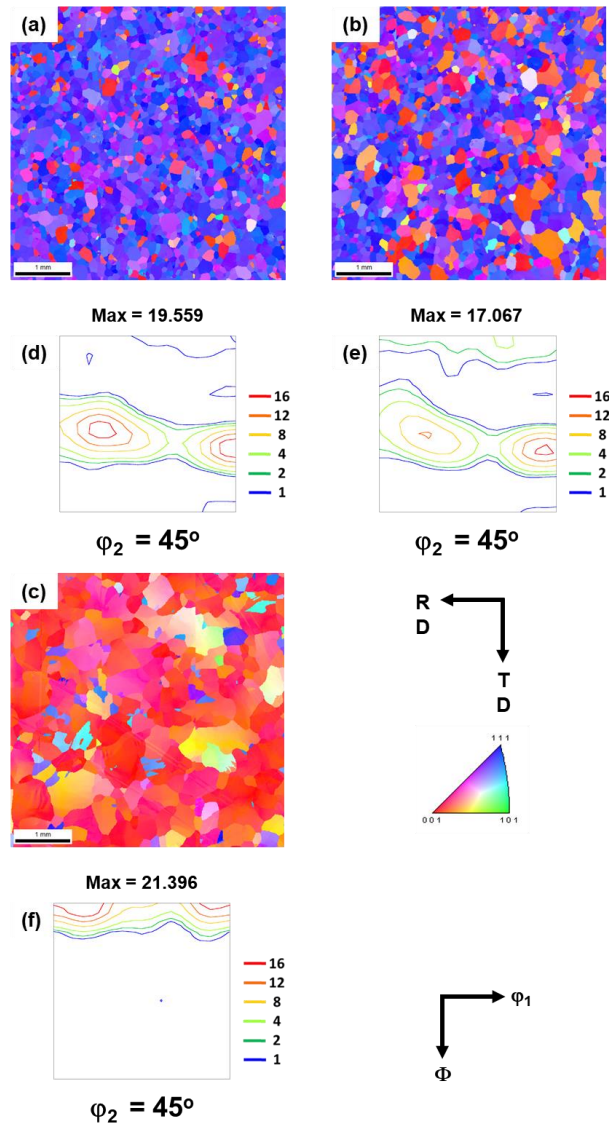


Fig. 2.7 EBSD IPF ND maps of the surface of Fe-2wt%Si-1wt%Ni after annealing at 1100 °C in H<sub>2</sub> for (a) 2 h, (b), 12 h and (c) 24 h. (d), (e) and (f) are ODFs at  $\varphi_2 = 45^\circ$  section for (a), (b) and (c), respectively.

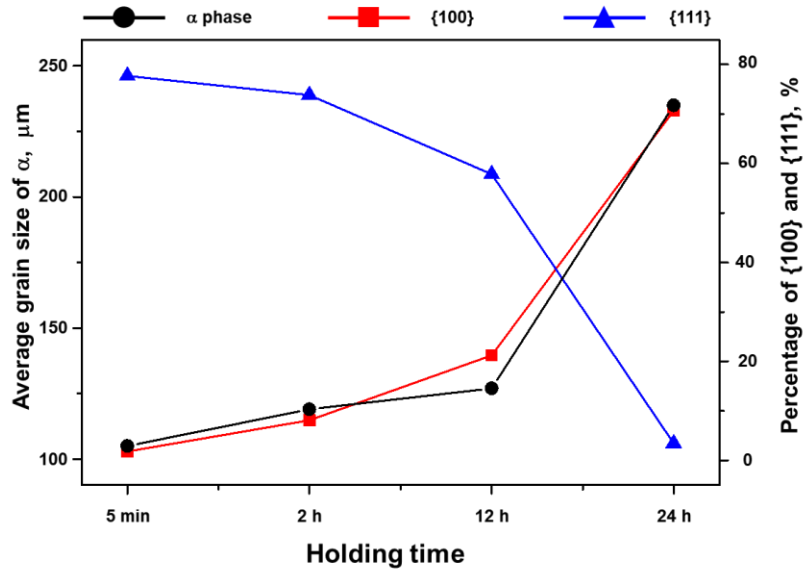


Fig. 2.8 Plots of the average  $\alpha$  grain size in IPF maps and percentages of {100} and {111} for Fe-2wt%Si-1wt%Ni against the heat treatment time.



# **Chapter 3. Uniaxial stress effect for the cube-on-face texture development during $\gamma \rightarrow \alpha$ phase transformation in Fe-2wt%Si-1wt%Ni electrical steel**

## **3.1. Experimental procedure**

Since chapter 2 shows that inducing stress on the surface of specimen is responsible for the texture development, a new method was devised to produce  $\{100\} \langle 0vw \rangle$  texture. Here, a specimen was placed with upright position to induce higher stress in a uniaxial direction, and the other specimen was placed with recumbent position to confirm the stress effect. In this chapter, it was studied how the compressive stress affects the texture evolution of  $\{100\} \langle 0vw \rangle$  in Fe-Si steel and a texture evolution could affect magnetic properties.

To check uniaxial compressive effect for the texture development, specimens of Fe-2wt%Si-1wt%Ni sheet with 80mm x 40mm x 0.35mm were prepared and were placed in different ways as shown in schematics of Fig. 3.1. One specimen was placed under the recumbent position on the nickel plate as shown in Fig. 3.1a, which takes negligible uniaxial stress on the cross-sectional area whereas another specimen was placed under the upright position as shown in Fig. 3.1b, which takes relatively higher uniaxial stress on the cross-sectional area. The reason why the specimen

with a recumbent position placed on the nickel plate is to minimize the differential thermal expansion coefficient effect on the contacted surface [36]. Specimens were heated to 1120 °C of the  $\gamma$  phase region at 10 °C/min, held for 1 min, 15 min, and 60 min, respectively, cooled to 970 °C for 120 min and cooled to room temperature in the furnace. To compare if the stress affects a grain growth whether during  $\gamma \rightarrow \alpha$  phase transformation or recrystallization, specimens were heated to 700 °C of recrystallization temperature at 10 °C/min, held for 60 min, cooled to room temperature in furnace.

To study the magnetic properties according to the texture development, three specimens with different percentages of  $\{100\}\langle 0vw \rangle$  and  $\{111\}\langle uvw \rangle$  were prepared. The first specimen was prepared by annealing at 1120 °C for 60 min by the upright position. The second specimen was placed on the nickel plate under the same heat treatment condition. The third specimen was prepared by the same way as the first specimen but annealing process underwent at 950 °C for 60 min, which is the  $(\alpha+\gamma)$  two phase region. Therefore, the  $\gamma \rightarrow \alpha$  transformation is not expected in the third specimen. The magnetic flux density at 5000 A/m ( $B_{50}$ ) and the core loss  $W_{15/50}$ , which was determined at a magnetic flux density of 1.5 T and 50 Hz, were measured by the MPG200D

instrument (BrockHaus Measurements). The dimension of the specimens to measure magnetic properties was 60 mm x 60 mm x 0.35 mm

**(a)**



**(b)**



Fig. 3.1 Schematic images of heat treatment conditions: (a) shows that the specimen is placed under recumbent position on the Ni plate. (b) shows that the specimen is placed under upright position.

### **3.2. Uniaxial stress effect for the development of cube-on-face texture**

Fig. 3.2a and d shows the inverse pole figure (IPF) ND map and the orientation distribution function (ODF) sectioned at  $\phi_2 = 45^\circ$  for the Fe-2wt%Si-1wt%Ni specimen heat treated under the recumbent position on the nickel plate at 1120 °C holding for 1 min, cooled to 970 °C for 120 min and cooled to room temperature in the furnace. Percentages of  $\{100\}\langle 0vw \rangle$  and  $\{111\}\langle uvw \rangle$  were 11.1% and 62.6%, respectively, which were determined using the criteria of  $\{100\}\langle 0vw \rangle \pm 15^\circ$ . Fig. 3.2b and e shows the IPF ND map and the ODF for the Fe-2wt%Si-1wt%Ni specimen heat treated under 1120 °C holding for 15 min, where the other condition was the same with Fig. 3.2a. Percentages of  $\{100\}\langle 0vw \rangle$  and  $\{111\}\langle uvw \rangle$  were 17.5% and 49.7%, respectively. Fig. 3.2c and f shows the IPF ND map and the ODF for the Fe-2wt%Si-1wt%Ni specimen heat treated under 1120 °C holding for 60 min, where the other condition was the same with Fig. 3.2a. Percentages of  $\{100\}\langle 0vw \rangle$  and  $\{111\}\langle uvw \rangle$  were 30.9% and 37.0%, respectively. The average grain sizes of Fig. 3.2a, b and c were 144  $\mu\text{m}$ , 156  $\mu\text{m}$  and 170  $\mu\text{m}$ , respectively, which was determined by converting the grain area into the diameter using an image analyzer software (EDAX/TSL software).

Fig. 3.3a and d shows the IPF ND map and the ODF for the Fe-2wt%Si-1wt%Ni specimen heat treated under the upright position at 1120 °C holding for 1 min, cooled to 970 °C for 120 min and cooled to room temperature in the furnace. Percentages of  $\{100\}\langle 0vw \rangle$  and  $\{111\}\langle uvw \rangle$  were 65.9% and 16.5%, respectively. Fig. 3.3b and e shows the IPF ND map and the ODF for the Fe-2wt%Si-1wt%Ni specimen heat treated under 1120 °C holding for 15 min, where the other condition was the same with Fig. 3.3a. Percentages of  $\{100\}\langle 0vw \rangle$  and  $\{111\}\langle uvw \rangle$  were 77.8% and 4.8%, respectively. Fig. 3.3c and f shows the IPF ND map and the ODF for the Fe-2wt%Si-1wt%Ni specimen heat treated under 1120 °C holding for 60 min, where the other condition was the same with Fig. 3.3a. Percentages of  $\{100\}\langle 0vw \rangle$  and  $\{111\}\langle uvw \rangle$  were 81.1% and 2.1%, respectively. The average grain sizes of Fig. 3.3a, b and c were 168  $\mu\text{m}$ , 196  $\mu\text{m}$  and 237  $\mu\text{m}$ , respectively. This aspect according to the specimen placement is plotted in Fig. 3.4, where the average grain size of  $\alpha$  is plotted against the holding time.

Fig. 3.2 and Fig. 3.3 show that entirely different texture was developed according to the specimen placement. Comparing the Fig. 3.2a and 3.3a, experiments were conducted under the same heat treatment condition, but the specimen placement was different which results in different texture development. The percentage of

$\{100\}\langle 0vw \rangle$  in Fig. 3.2a was 11.1 % but the percentage of  $\{100\}\langle 0vw \rangle$  in Fig. 3.3a was 65.9%. The percentage of  $\{100\}\langle 0vw \rangle$  texture in Fig. 3.2 was increased from 11.1% to 17.5% and 30.9% as increased holding time, but dominant texture was  $\gamma$  fiber. In the case of the Fig. 3.3, however, the percentage of  $\{100\}\langle 0vw \rangle$  texture was increased from 65.9% to 77.8% and 81.1% as increased holding time. The  $\{100\}\langle 0vw \rangle$  of both Fig. 3.2 and Fig. 3.3 have increasing tendency but the major texture was different. This aspect is plotted in Fig. 3.5, where the percentage of  $\{100\}\langle 0vw \rangle$  and  $\{111\}\langle uvw \rangle$  are plotted against holding time.

The chapter2 shows strong cube-on-face texture development using self-load method during heat treatment. A strong  $\{100\}\langle 0vw \rangle$  texture was developed using Fe-1wt%Si at 1100°C holding for 5 min. However, a strong  $\gamma$  fiber texture was developed when the component was changed to Fe-2wt%Si-1wt%Ni under the same condition, which result was interpreted in terms of the grain size effect. If a specimen has smaller grain size during  $\gamma$  phase region, the probability of surface nucleation would be lower, however, if a specimen has larger grain size during  $\gamma$  phase region, the probability of surface nucleation would be higher than smaller grain size. Therefore, to enhance a probability of the surface nucleation, a holding time was increased under  $\gamma$  phase

region. Then, the texture development was changed from the strong  $\gamma$  fiber texture to the strong  $\{100\}$  texture when the annealing time was increased from 5 min to 24 h, which result coincided with the grain size effect.

Our group assumed that such a different texture development between the Fig. 3.2 and Fig. 3.3 is related to the applying stress for the specimen, which could affect grain growth during  $\gamma \rightarrow \alpha$  phase transformation. Comparing the receiving stress on the center area of each specimen, the compressive stress applied to the cross-sectional area of Fig. 3.1a is 13.5 Pa whereas Fig. 3.2a is 1210 Pa, which has a 100 times disparity. When BCC  $\alpha$  nucleates form FCC  $\gamma$ , the nucleus would be under the compressive stress and the strain energy is proportional to the Young's modulus or the shear modulus. Therefore, if one nucleus is formed under high compressive stress as shown in Fig. 3.1b, nucleation barrier would be larger whereas nucleation barrier would be smaller when the nucleus is under lower compressive stress as shown in Fig. 3.1a. Thus, during  $\gamma \rightarrow \alpha$  phase transformation, the probability of the surface nucleation would be higher under the upright position because all the nuclei, which are including four grain corners and triple junctions, are under the higher compressive stress. However, a probability of the bulk nucleation would be higher under the



recumbent position because all the nuclei, which are including four grain corners and triple junctions, are under the lower compressive stress. Thus, different texture evolution comes from the differences in compressive stress.

Fig. 3.6a and c shows the IPF ND map and the ODF the Fe-2wt%Si-1wt%Ni specimen heat treated under the recumbent position on the nickel plate at 700 °C holding for 60 min, cooled to room temperature in the furnace. Percentages of  $\{100\}\langle 0vw \rangle$  and  $\{111\}\langle uvw \rangle$  were 6.5% and 61.0%, respectively. Fig. 3.6b and d shows the IPF ND map and the ODF the Fe-2wt%Si-1wt%Ni specimen heat treated under the upright position at 700 °C holding for 60 min, cooled to room temperature in the furnace. Percentages of  $\{100\}\langle 0vw \rangle$  and  $\{111\}\langle uvw \rangle$  were 9.7% and 57.1%, respectively. The average grain sizes of Fig. 3.6a and b were 17.5  $\mu\text{m}$  and 18.4  $\mu\text{m}$ , respectively.

There are two possible points for the grain growth by compressive stress. If the stress influences under the recrystallization temperature, the grain size of upright position would be larger. If not, the final grain size was affected during  $\gamma \rightarrow \alpha$  phase transformation. To confirm the compressive stress affects a grain growth whether during  $\gamma \rightarrow \alpha$  phase transformation or recrystallization, a heat treatment was conducted under the

recrystallization temperature. The result of Fig. 3.6 shows that the texture development and grain size have a similar range, which indicates that the point of the grain growth is not the recrystallization but the  $\gamma \rightarrow \alpha$  phase transformation.

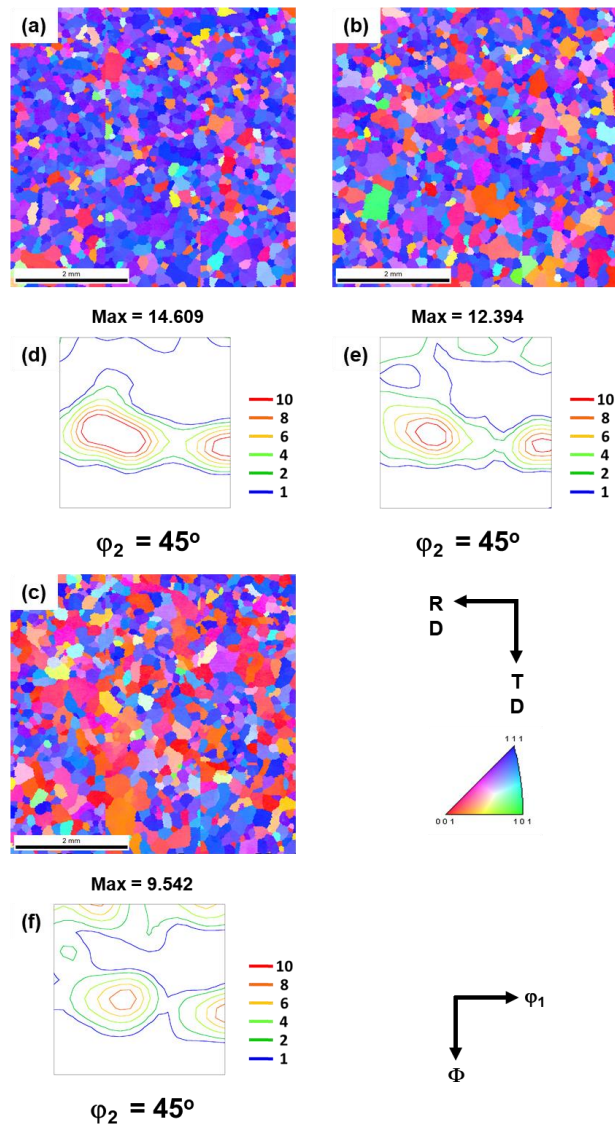


Fig. 3.2 EBSD inverse pole figure ND maps of Fe-2wt%Si-1wt%Ni specimens were placed under the recumbent position on the nickel plate annealed at 1100 °C in H<sub>2</sub> for (a) 1 min, (b), 15 min and (c) 60 min. (d), (e) and (f) are ODFs at  $\varphi_2 = 45^\circ$  section for (a), (b) and (c), respectively.

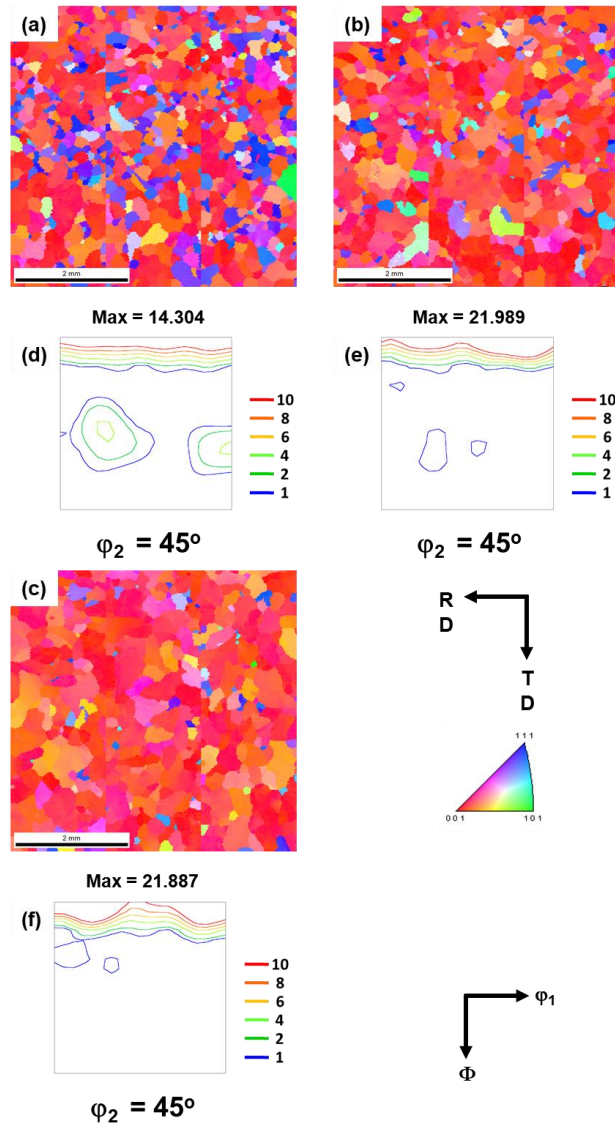


Fig. 3.3 EBSD inverse pole figure ND maps of Fe-2wt%Si-1wt%Ni specimens were placed under the upright position annealed at 1100 °C in H<sub>2</sub> for (a) 1 min, (b), 15 min and (c) 60 min. (d), (e) and (f) are ODFs at  $\varphi_2 = 45^\circ$  section for (a), (b) and (c), respectively.

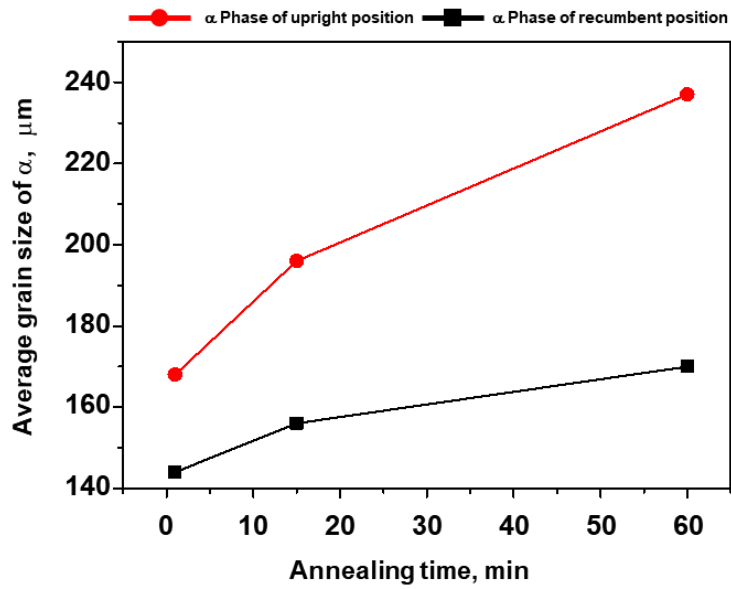


Fig. 3.4 plot of the average  $\alpha$  grain size against the annealing time under different specimen placement.

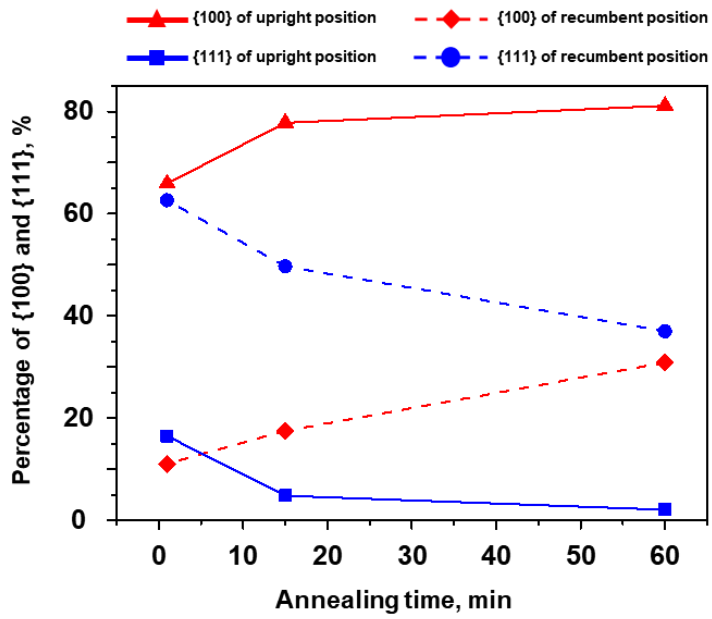


Fig. 3.5 plot of {100} and {111} texture development against the annealing time under different specimen placement.

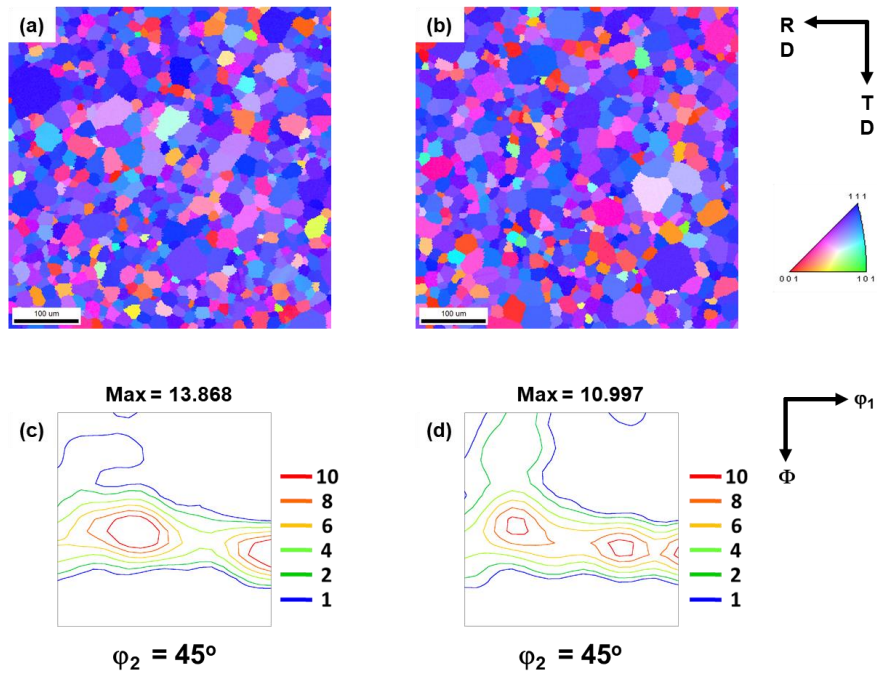


Fig. 3.6 EBSD inverse pole figure ND maps of Fe-2wt%Si-1wt%Ni specimens annealed at 1100 °C for 60min in H<sub>2</sub>: (a) the specimen was placed under the recumbent position on the nickel plate, (b) the specimen was placed under the upright position. (c) and (d) are ODFs at  $\varphi_2 = 45^\circ$  section for (a) and (b), respectively.

### 3.3. Magnetic properties by a texture development

To study how the magnetic properties could be affected by a texture development under the same chemical composition of Fe–2wt%Si–1wt%Ni specimens. Three types of texture controlled specimens were prepared, which were controlled using the stress and temperature.

Fig. 3.7a and d shows the IPF ND map and the ODF for the Fe–2wt%Si–1wt%Ni specimen heat treated under the upright position at 1120 °C holding for 60 min, cooled to room temperature in the furnace. Percentages of  $\{100\}\langle 0vw \rangle$  and  $\{111\}\langle uvw \rangle$  were 78.4% and 3.2%, respectively. Fig. 3.7b and e shows the IPF ND map and the ODF for the Fe–2wt%Si–1wt%Ni specimen heat treated under the recumbent position, where the other condition was the same with Fig. 3.7a. Percentages of  $\{100\}\langle 0vw \rangle$  and  $\{111\}\langle uvw \rangle$  were 35.6% and 26.9%, respectively. Fig. 3.7c and f shows the IPF ND map and the ODF for the Fe–2wt%Si–1wt%Ni specimen heat treated under 950 °C holding for 60 min, cooled to room temperature in the furnace. Percentages of  $\{100\}\langle 0vw \rangle$  and  $\{111\}\langle uvw \rangle$  were 0.7% and 81.3%, respectively. The average grain sizes of Fig. 3.7a, b and c were 235  $\mu\text{m}$ , 170  $\mu\text{m}$  and 127  $\mu\text{m}$ , respectively.

Fig. 3.7a has the maximum percentage, 78.4% of  $\{100\}\langle 0vw \rangle$ ,



and 3.2% of  $\{111\}\langle uvw \rangle$  which produces the highest magnetic flux density of  $B_{50} = 1.75$  and the lowest iron loss of  $W_{15/50} = 2.19$ . Fig. 3.7b has 35.6% of  $\{100\}\langle 0vw \rangle$  and 26.9% of  $\{111\}\langle uvw \rangle$ , which produces  $B_{50} = 1.69$  and  $W_{15/50} = 2.34$ . Fig. 3.7c has 0.7% of  $\{100\}\langle 0vw \rangle$  and 81.3% of  $\{111\}\langle uvw \rangle$ , which produces  $B_{50} = 1.61$  and  $W_{15/50} = 2.50$ . Therefore, the magnetic properties strongly depend on the percentage of  $\{100\}\langle 0vw \rangle$ .

Fig. 3.8 shows the comparison of magnetic properties. When comparing specimens of the same composition, as the percentage of  $\{100\}\langle 0vw \rangle$  increases,  $B_{50}$  increases and  $W_{15/50}$  decreases. In the case of the specimen with  $\{100\}\langle 0vw \rangle$  of 0.7%, the  $B_{50}$  was lower than 35PN270, which composition is about 3wt%Si, and the  $W_{15/50}$  had higher values. But when the  $\{100\}\langle 0vw \rangle$  increased to 35.6%, the specimen exhibited better magnetic properties than 35PN270. These results indicate that magnetic properties such as  $B_{50}$  and  $W_{15/50}$  are strongly depended on the texture development.

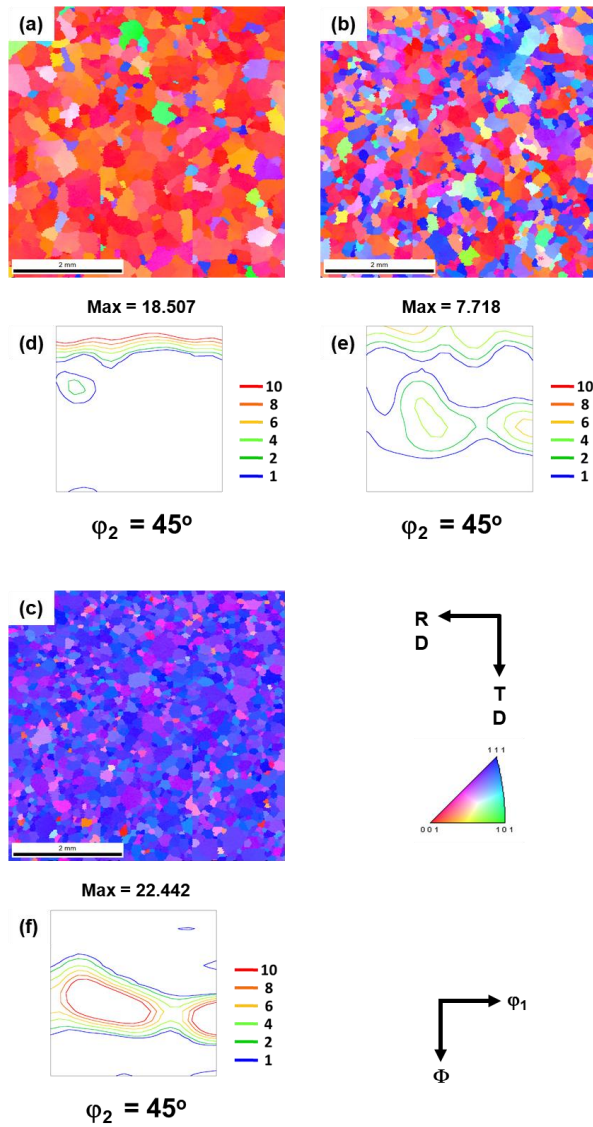


Fig. 3.7 EBSD inverse pole figure ND maps of Fe-2wt%Si-1wt%Ni specimen to confirm the relationship between magnetic properties and the (100) texture development. (a) 78.4% of (100), (b) 35.6% of (100) and (c) 0.7% of (100). (d), (e) and (f) are ODFs at  $\phi_2 = 45^\circ$  section for (a), (b) and (c), respectively.

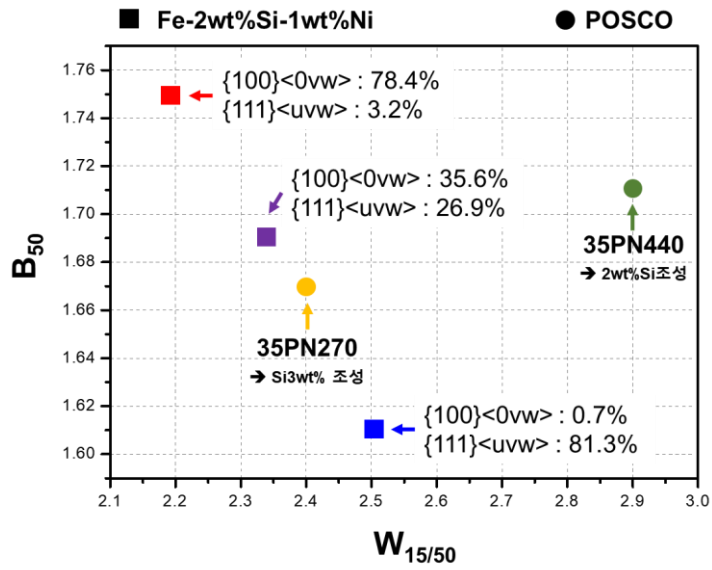


Fig. 3.8 Plots for the magnetic properties of specimens with controlled texture and commercial non-oriented electrical steel.

# **Chapter 4. Texture evolution of non-oriented electrical steel analyzed by EBSD and in-situ XRD during the phase transformation from $\gamma$ to $\alpha$**

## **4.1. Experimental procedure**

Our preliminary experiments indicate that as the content of alloying elements increases, it gets more difficult to control the texture. The exact phase diagram to design a suitable heat treatment, the phase boundary or the solvus line of  $\gamma$  is important. For the texture control, the information which orientation is nucleated and grow dominantly during cooling is very important. To determine such information, we used in-situ X-ray diffraction (XRD) during heating and cooling of the two specimens of Fe-2wt%Si-1wt%Ni and Fe-3wt%Si-2.5wt%Ni. The analysis was focused on why the Fe-2wt%Si-1wt%Ni specimen has the dominant  $\{100\}$  texture whereas the Fe-3wt%Si-2.5wt%Ni specimen has the dominant  $\{112\}$  texture even though the two specimens undergo the same heat treatment.

For the electron back-scattered diffraction (EBSD, EDAX / Hikari) analysis, the specimens were heated to 1100 °C for 2 h, held for 4 h, cooled to 950 °C for 2 h under flowing  $H_2$ , and then cooled in the furnace to room temperature. For the heat treatment, an electric furnace with a quartz tube was used. A quartz tube tends

to deform above 1100 °C, which becomes the upper limit of the heat treatment. Heating and cooling of the specimen in the tube furnace was controlled by the proportional, integral and derivative (PID) controller. For furnace cooling, the power of the tube furnace was turned off.

To observe the phase transformation during heating and cooling, the specimens were examined using in-situ X-ray diffractometer (XRD, PANalytical / X' pert Pro MPD) with a Cu K $\alpha$  ( $\lambda = 1.5418 \text{ \AA}$ ) with the 2-theta range of 20° ~ 90°. As-cold rolled specimens were cut into with 18mm diameter to fit into the XRD holder. The in-situ XRD was equipped with a hot stage up to 1200 °C under controlled atmospheric conditions. In the heating condition, the stage was heated from 400 °C to 1200 °C at an interval of 50 °C with 60 min dwelling time to get a sufficient signal. At 1200 °C, the stage was held for 180 min for homogenization of the specimen. In the cooling condition, the stage was cooled from 1200 °C to 400 °C at an interval of 50 °C with 60 min dwelling time.

To protect the specimen from being oxidized, measurements were conducted under Ar 90% + H<sub>2</sub> 10%. It should be noted that 100% H<sub>2</sub> cannot be used in the in-situ XRD system. Specimens of 15 x 30 mm<sup>2</sup> for the EBSD analysis were prepared to examine the texture evolution. The surface of all specimens was polished to the

final stage using a solution of colloidal silica (OP-s, 0.04  $\mu\text{m}$ ).

## 4.2. Results & Discussion

Fig. 4.1 shows the EBSD analysis of Fe-2wt%Si-1wt%Ni and Fe-3wt%Si-2.5wt%Ni heating at 1100 °C for 4 h under flowing H<sub>2</sub>. Drastically different textures were evolved between the specimens. The inverse pole figure (IPF) maps in Fig. 4.1a and b shows crystal orientations using colors designated in the stereo-projection triangle shown in the right of Fig. 4.1. In the stereo-projection triangle in Fig. 4.1, the <100> direction is designated by the red color. Thus, the red color in the IPF map represent grains of the cube orientations {100}<0vw>. As a result, the high fraction of red colored grains in the IPF maps represent the high fraction of {100}<0vw>. Accordingly, the fraction of {100}<0vw> is much higher in Fig. 4.1a than in Fig. 4.1b. The quantitative data for the area fraction of the cube orientation were determined using the criteria of {100}<0vw> ± 15° from the raw data of the IPF map.

In the orientation distribution functions (ODF) in Fig. 4.1c and d, the Euler angle ( $\varphi_1$ ,  $\Phi$ ,  $\varphi_2$ ) of each grain, which represents the grain orientation, is plotted on the coordinate of  $\varphi_1$  and  $\Phi$  at  $\varphi_2 = 45^\circ$  section. In the ideal cube texture, the Euler angles of grains would be distributed along  $\Phi = 0$  in the ODF. The ODF in Fig. 4.1c shows a much higher intensity of grain orientations, whose Euler angles lie

along  $\Phi = 0$ , than that in Fig. 4.1d, indicating that the intensity of  $\{100\} \langle 0vw \rangle$  is much higher in Fig. 4.1c than in Fig. 4.1d.

The IPF map and ODF of the Fe-2wt%Si-1wt% specimen in Fig. 4.1a and c shows the strong  $\{100\}$  texture, respectively. Percentages of  $\{100\}$  and  $\{112\}$  are, respectively, 56.9% and 10.8%. The percentage of  $\{112\}$  was determined using the criteria of  $\{112\} \pm 15^\circ$ . The average grain size 252  $\mu\text{m}$  which was determined by converting the grain area into the diameter. In comparison, the IPF map and ODF of the Fe-3wt%Si-2.5wt%Ni specimen, respectively, in Fig. 4.1b and d shows the strong  $\{112\}$  texture. Percentages of  $\{100\}$  and  $\{112\}$  were, respectively, 0.6% and 85.7%. The average grain size was 252  $\mu\text{m}$ .

Fig. 4.2 and Fig. 4.3 show XRD peaks for the Fe-2wt%Si-1wt%Ni specimen during heating from 400  $^\circ\text{C}$  to 1200  $^\circ\text{C}$  and during cooling from 1200  $^\circ\text{C}$  to 400  $^\circ\text{C}$ , respectively. When the temperature was increased from 400  $^\circ\text{C}$  to 800  $^\circ\text{C}$ , the ferrite peaks of  $\alpha\text{-}\{011\}$ ,  $\alpha\text{-}\{002\}$ , and  $\alpha\text{-}\{112\}$  persisted. However, when the temperature was increased to 900  $^\circ\text{C}$ , the peak of  $\alpha\text{-}\{011\}$  disappeared and only the peak of  $\alpha\text{-}\{112\}$  950  $^\circ\text{C}$  remained. Afterwards, the  $\alpha$ -phase disappeared at temperature higher than 1000  $^\circ\text{C}$  as shown in Fig. 4.2. In the case of the austenite phase,  $\gamma\text{-}\{111\}$ ,  $\gamma\text{-}\{002\}$ , and  $\gamma\text{-}\{220\}$  appeared simultaneously at 900  $^\circ\text{C}$ , and the peak intensity



ratio of each orientation was changed as the temperature increased. Especially, the intensity ratio of  $\gamma$ - $\{111\}$  to  $\gamma$ - $\{002\}$  was changed in the temperature range of 950 °C ~ 1000 °C. Fig. 4.3 shows the XRD peaks during cooling, where the ferrite  $\alpha$  did not appear until the temperature was decreased to 1000 °C.  $\alpha$ - $\{002\}$  and  $\alpha$ - $\{112\}$  appeared at 950 °C simultaneously, and  $\alpha$ - $\{011\}$  appeared at 900 °C. As the temperature decreased, the peak intensity ratio was changed.  $\gamma$ - $\{111\}$ ,  $\gamma$ - $\{002\}$ , and  $\gamma$ - $\{220\}$  remained until the temperature was decreased to 500 °C.

Fig. 4.4 and Fig. 4.5 show the XRD peaks of the Fe-3wt%Si-2.5wt%Ni specimen under the same heat cycle. During heating,  $\alpha$ - $\{011\}$  disappeared first at 900 °C and then  $\alpha$ - $\{002\}$  disappeared at 1000 °C but  $\alpha$ - $\{112\}$  remained until 1200 °C as shown in Fig. 4.4. In the case of the austenite phase,  $\gamma$ - $\{111\}$ ,  $\gamma$ - $\{002\}$ , and  $\gamma$ - $\{220\}$  appeared simultaneously. Fig. 4.5 shows the XRD peaks during cooling,  $\alpha$ - $\{112\}$  appeared first at 900 °C. Then,  $\alpha$ - $\{011\}$  and  $\alpha$ - $\{002\}$  appeared at 700 °C, and the peak intensity ratio was changed as the temperature decreased. All the peaks of the austenite phase disappeared below 800 °C, whose aspect is different from that of the Fe-2wt%Si-1%Ni specimen.

During heating, all the peaks of Fig. 4.2 and Fig. 4.4 are slightly shifted to the left. This decrease of  $2\theta$  corresponds to the increase

of the 'd' spacing from the Bragg's law of  $n\lambda = 2d \sin\theta$ . The increase of the 'd' spacing corresponds to the increase of the lattice parameter, which would come from the thermal expansion of the specimen during heating. Likewise, during cooling, all the peaks of Fig. 4.3 and Fig 4.5 are slightly shifted to the right. This increase of  $2\theta$  corresponds to the decrease of the 'd' spacing, which would be caused by the thermal contraction of the specimen during cooling.

The evolution of the  $\{100\}$  texture can be examined by comparing the XRD peak intensity ratio of our specimen with that of the random texture reported in the reference [41] as shown in Fig. 4.6. If any material has a strong texture, which is revealed by the intensity of specific peaks at corresponding  $2\theta$ , it would be stronger than of the random texture. In order to determine which orientation nucleates preferentially during the phase transformation from  $\gamma$  to  $\alpha$ , the intensity of the in-situ XRD peaks was compared with that of the random in Fig. 4.6 [41]. Fig. 4.6a shows that during cooling of the Fe-3wt%Si-2.5wt%Ni specimen, the peak of  $\alpha$ - $\{112\}$  appeared exclusively at 900 °C with the peaks of  $\alpha$ - $\{011\}$  and  $\alpha$ - $\{002\}$  being absent. The peaks of  $\alpha$ - $\{011\}$  and  $\alpha$ - $\{002\}$  appeared at 700 °C. Comparing the peak intensity of the Fe-3wt%Si-2.5wt%Ni specimen with that of the random texture, the peak of  $\alpha$ - $\{112\}$  of the Fe-3wt%Si-2.5wt%Ni specimen is significantly

higher and the peak of  $\alpha$ -{011} is relatively lower than those of the random texture. The peak intensity ratio was maintained down to 400 °C as shown in Fig. 4.6a

In the case of the Fe-2wt%Si-1wt%Ni specimen, Fig. 4.6b shows that the peak of  $\alpha$ -{002} was most dominant during cooling at 950 °C although the peak of  $\alpha$ -{011} coexisted. It should be noted that the peak intensity of  $\alpha$ -{002} of the Fe-2wt%Si-1wt%Ni specimen at 950 °C is 6 times stronger than that of the random texture whereas the  $\alpha$ -{112} peak intensity at 950 °C is about twice stronger than that of the random texture. Fig. 4.6b shows that the peak of  $\alpha$ -{011} began to appear at 800 °C and became stronger at 400 °C. As the temperature decreased from 950 °C to 800 °C, the peak intensities of  $\alpha$ -{002} and  $\alpha$ -{112}, respectively, decreased and increased slightly. Their peak intensities did not change at 400 °C.

Although the two specimens of Fe-3wt%Si-2.5wt%Ni and Fe-2wt%Si-1wt%Ni underwent the same heat treatment, quite a different texture was evolved. The two specimens differ in the content of Si and Ni. To reduce the core loss in electrical steel, the resistivity should be increased, which is achieved by increasing the silicon content. The austenite stabilizing element such as nickel is needed for  $\alpha \rightarrow \gamma$  transformation during heating.

The exclusive peak of  $\alpha$ -{112} at 900 °C and its dominance throughout cooling of the Fe-3wt%Si-2.5wt%Ni specimen shown in Fig. 4.5 and Fig. 4.6a would be responsible for the evolution of the strong {112} texture shown in Fig. 4.1b. The dominant peak of  $\alpha$ -{002} of the Fe-2wt%Si-1wt%Ni specimen during cooling at 950 °C shown in Fig. 4.3b and Fig. 4.6b would be responsible for the evolution of the strong {002} texture shown in Fig. 4.1a. However, in-situ XRD peaks of Fig. 4.3 and Fig. 4.6b show that the peak of  $\alpha$ -{112} became stronger than that of  $\alpha$ -{002} as the temperature decreased to 400 °C.

These XRD peaks of the Fe-2wt%Si-1wt%Ni specimen do not match with the EBSD IPF map in Fig. 4.1a and the 45° section of ODF in Fig. 4.1c, where percentages of {100} and {112} are, respectively, 56.9% and 10.8%. There are two possible sources for these evolutions. One is the difference in the austenizing temperature among Fig. 4.1, Fig. 4.2 and Fig. 4.3. For the specimen in Fig. 4.1, it was 1100 °C but for in-situ XRD measurements in Fig. 4.2 and Fig. 4.3, it was 1200 °C. The other is the difference in the cooling condition. The Fig. 4.1 specimen was continuously cooled from 1100 °C to 950 °C for 2 h and then cooled to room temperature in the furnace. However, for in-situ XRD measurements, the stage was cooled from 1200 °C to 400 °C at an

interval of 50 °C with 60 min dwelling time.

It is clearly understood that the dominant cube texture of Fig. 4.1a is related with the dominant  $\{200\}$  peak of Fig. 4.3 and Fig. 4.6b. However, it is not clearly understood why the Fe-2wt%Si-1wt%Ni specimen had the dominant cube texture as shown in Fig. 4.1a whereas the Fe-3wt%Si-2.5wt%Ni specimen had the dominant  $\gamma$ -fiber texture as shown in Fig. 4.1b.

One possibility for such drastically different textures evolution with a composition change is that the Fe-2wt%Si-1wt%Ni specimen is in the single  $\gamma$  phase region at 1100 °C whereas the Fe-3wt%Si-2.5wt%Ni specimen is in the  $(\alpha + \gamma)$  two phase region the same temperature, which would be just below the solvus line of the  $\gamma$  phase. This is supported by in-situ XRD data in Fig. 4.2 and Fig. 4.4. Fig. 4.2 shows that the peak of  $\alpha$ - $\{112\}$ , which existed at 950 °C, disappeared at 1000 °C during heating. This means that 1100 °C is the  $\gamma$  single phase region for the Fe-2wt%Si-1wt%Ni specimen. However, Fig. 4.4 shows that the peak of  $\alpha$ - $\{112\}$ , which existed at 1100 °C, disappeared at 1200 °C during heating. This means that 1100 °C is the  $(\alpha + \gamma)$  two phase region for the Fe-3wt%Si-2.5wt%Ni specimen.

Then, why does the dominant formation of the texture depend on whether the specimen is heated to the  $\gamma$  one phase region or to

the ( $\alpha + \gamma$ ) two phase region? If the alloy is heated to the ( $\alpha + \gamma$ ) two phase region and cooled, the  $\alpha$  phase need not be nucleated because the grains of the  $\alpha$  phase already exist. The  $\gamma$  phase would be consumed by the growth of the pre-existing  $\alpha$  phase. In this case, the texture would depend on the major orientation of the remaining  $\alpha$  phase at 1100 °C, which seems to be  $\alpha$ -{112} for the Fe-3wt%Si-2.5wt%Ni specimen.

If the alloy is heated to the  $\gamma$  single phase region and cooled, however, the  $\alpha$  phase needs to be nucleated. The  $\alpha$  orientation, which has the lowest nucleation barrier, would be nucleated. Then, which orientation would have the lowest nucleation barrier? Since the volume expands when the bcc  $\alpha$  nucleates from the fcc  $\gamma$ , the strain energy should be considered. Since the strain energy is proportional to the Young's modulus, the orientation with the minimum Young's modulus would have the lowest strain energy. It is known that the  $\langle 100 \rangle$  direction has the lowest Young's modulus in the bcc Fe [32]. Therefore, if the appropriate 2-dimension tensile stress is applied to the surface of the specimen during the phase transformation from  $\gamma$  to  $\alpha$  during cooling, it will favor the surface nucleation of  $\alpha$  with {100}. This effect was studied experimentally in detail by Kwon et al. [33]. Thus, under the 2-dimensional stress condition, the {100} grains would have the

lowest strain energy. If  $\alpha$  nucleates at the surface of the specimen, it would be under the 2-dimensional stress condition and then the  $\{100\}$  grains would have the lowest strain energy. This might be why the Fe-2wt%Si-1wt%Ni specimen had the dominant  $\{100\}$  texture as shown in Fig. 4.1a after being cooled from 1100 °C.

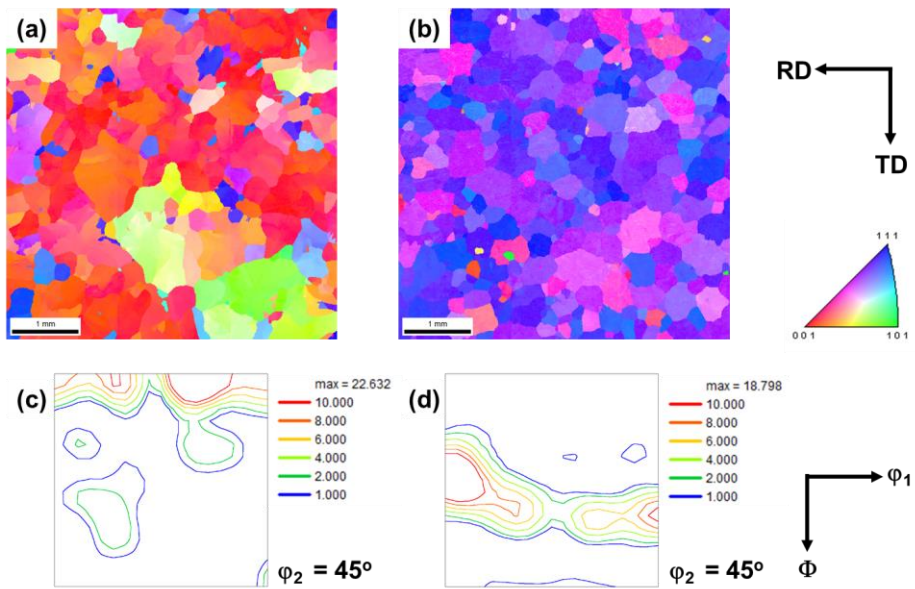


Fig. 4.1 EBSD inverse pole figure ND maps of (a) Fe-2wt%Si-1wt%Ni and (b) Fe-3wt%Si-2.5wt%Ni and  $45^\circ$  sections of ODF of (c) Fe-2wt%Si-1wt%Ni and (d) Fe-3wt%Si-2.5wt%Ni after the specimens were annealed at 1100 °C for 4 h under flowing  $H_2$ .



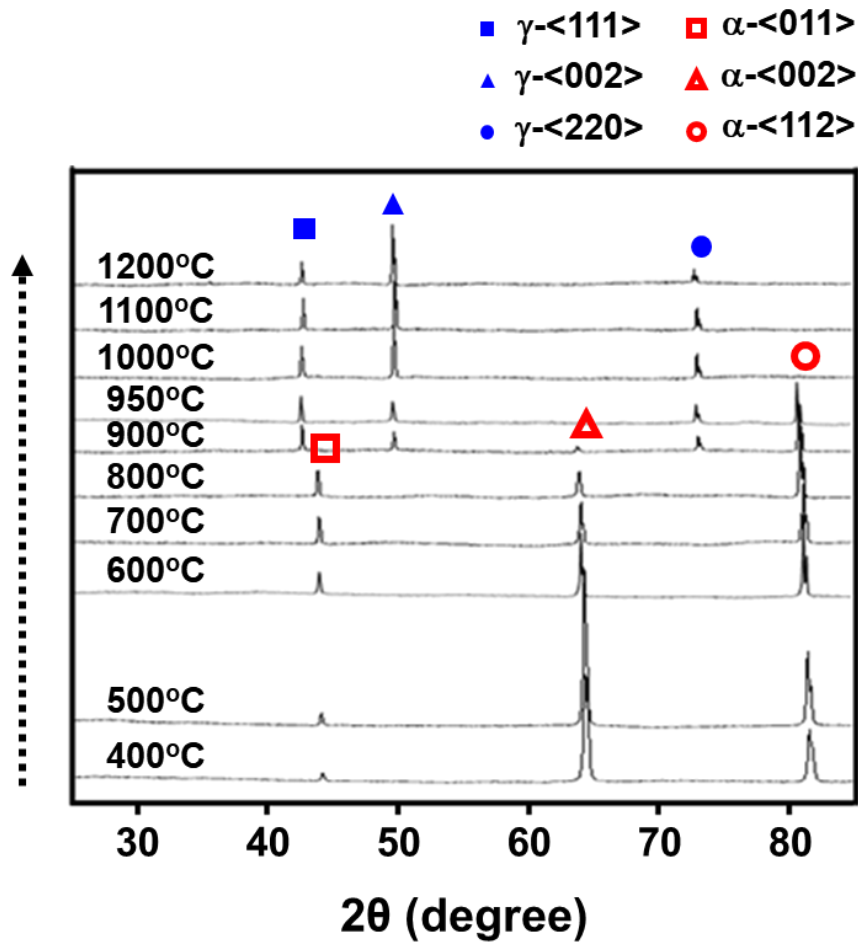


Fig. 4.2 In-situ XRD peaks of Fe-2%Si-1%Ni during heating from 400 °C to 1200 °C.

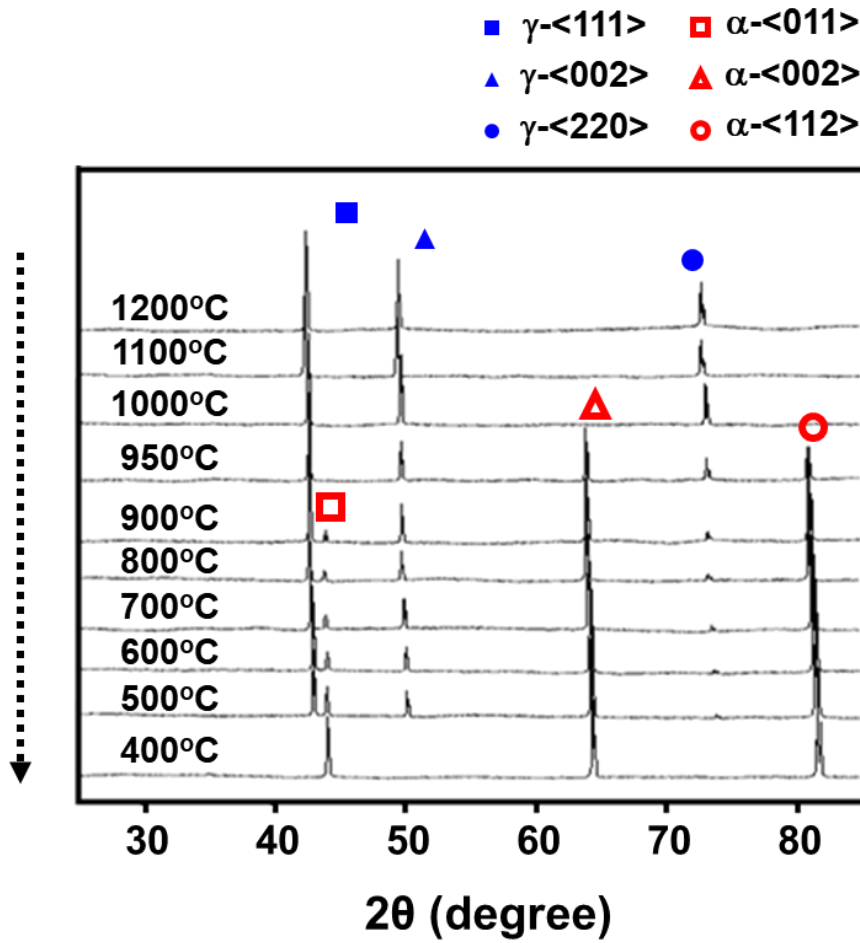


Fig. 4.3 In-situ XRD peaks of Fe-2%Si-1%Ni during cooling from 1200 °C to 400 °C.

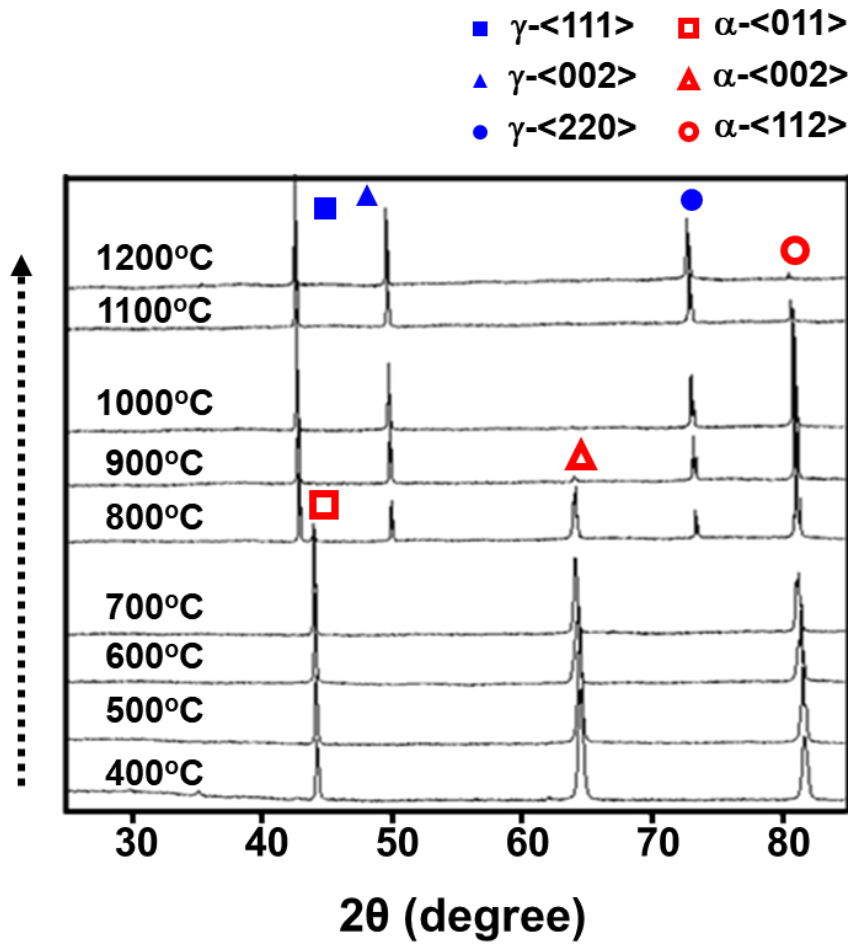


Fig. 4.4 In-situ XRD peaks of Fe-3%Si-2.5%Ni during heating from 400 °C to 1200 °C.

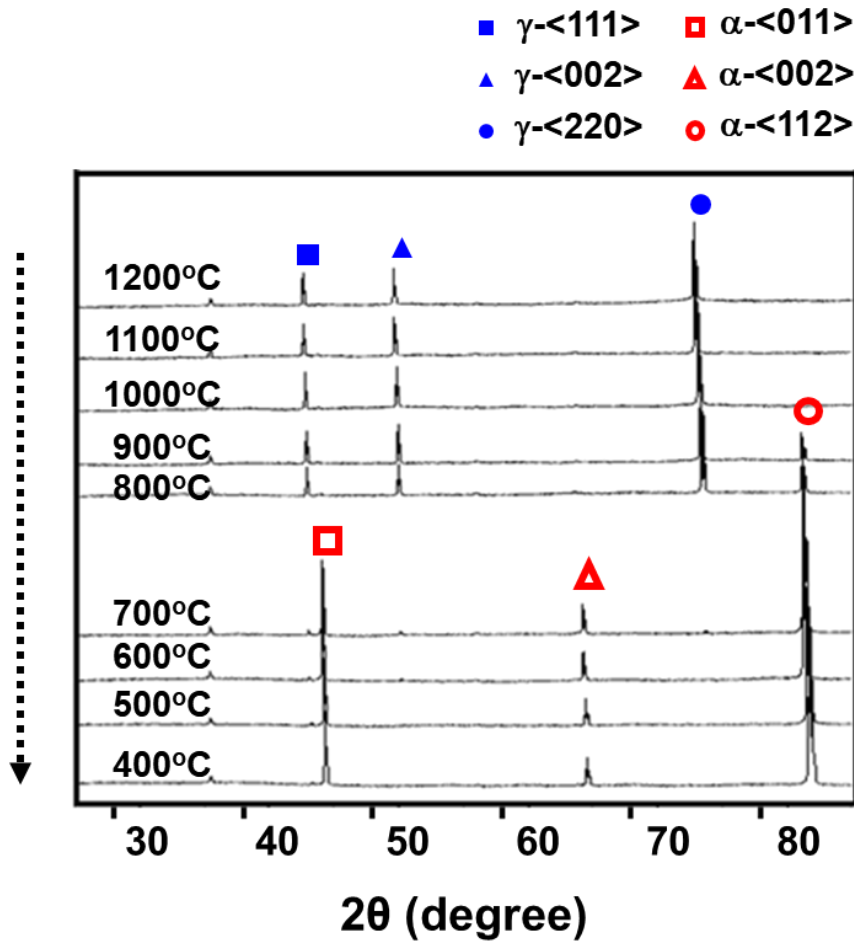


Fig. 4.5 In-situ XRD peaks of Fe-3%Si-2.5%Ni during cooling from 1200 °C to 400 °C.

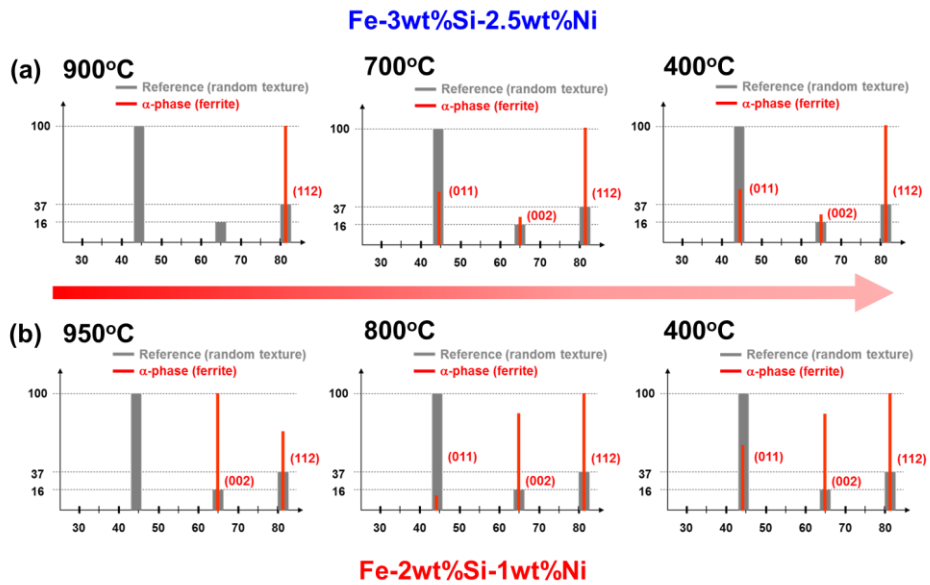


Fig. 4.6 Comparison of the XRD peak intensity during cooling of the specimens with those of the powder of the same composition (a) for Fe-3wt%Si-2.5wt%Ni and (b) for Fe-2wt%Si-1wt%Ni.

# **Chapter 5. A new method for the evolution of strong cube-on-face texture induced by $\gamma \rightarrow \alpha$ phase transformation with the silicon diffusion in Fe-Si electrical steel**

## **5.1. Introduction**

The silicon is key element to reduce the core loss, therefore increasing silicon content is quite important in electrical steel. However, increasing silicon content made the material brittle [42–44]. Therefore, the silicon content should be limited about 3wt% to progress a cold rolling process. There are some references [15, 45–48] using the silicon diffusion into the electrical steel, but, base materials of which are not including  $\gamma$  phase at high temperature, which couldn't induce  $\gamma \rightarrow \alpha$  phase transformation, or the annealing process was conducted under  $\gamma$  phase temperature. In this chapter, however, based on the surface nucleation could affect  $\{100\} \langle 0vw \rangle$  generation on the specimen surface, a new method is devised using silicon content.

## 5.2. Experimental procedure

An ingot of Fe–1wt%Si, which was manufactured by vacuum induction melting, was prepared as a starting material. The ingot was hot rolled to 2.3 mm and cold rolled to 0.35 mm thickness. Boron doped <100> single crystal silicon wafer was prepared as a diffusion source. The specimen size of Fe–1wt%Si sheet for heat treatment was 15mm x 30mm x 0.35mm and 10mm x 25mm x 0.6mm of silicon wafer was placed on the Fe–1wt%Si sheet, they were contacted each other as shown in Fig. 5.4.

The Fe–1wt%Si sheet specimen without contact any materials, which was prepared to compare with the Si diffusion specimens, was heated to 1100 °C for 2 h, held for 5 min, cooled to 950 °C for 2 h under flowing H<sub>2</sub>, and then cooled in the furnace to room temperature. To induce silicon diffusion, the Fe–1wt%Si sheet specimen was in contact with a silicon wafer and the heat treatment was conducted under the same condition. Then, the others were changed the holding temperature to 1050 °C and 1000 °C with the other experimental conditions being the same as those of the 1100 °C condition. Here we designate these annealing process as slow cooling conditions except for annealing temperature.

Since the highest percentage of the cube-on-face texture was obtained under the 1100 °C condition of contact with the silicon

wafer, more systemic experiments for the time were performed. Specimens were in contact with silicon wafer and experiments were conducted under the method of in and out condition holding for 2 min, 4min, 7.5 min, 15 min, 30 min, and 60 min, respectively. And, we also designate these annealing processes as in and out conditions except for holding time.

The phase transformation temperature of Fe–1wt%Si specimen was measured under the heating rate of 10 °C/min with the thermo–gravimetric analysis (TGA)/differential scanning calorimetry (DSC, Mettler Toledo). The measured temperatures for  $A_{c1}$ ,  $A_{c3}$  of the Fe–1wt%Si specimen were, respectively, 987 °C and 999 °C as shown in Fig. 5.1. Elemental components of Si and Fe were determined by The X–ray fluorescence (XRF, M4 Tornado/Bruker) inspector. The spectrum of each specimen was acquired for 300s real time at tube setting of 50 kV and 0.6mA with 1 mm x 0.5 mm area.

To confirm the diffusion effect of a Si powder, a commercially pure Si powder, which is less than –325 mesh ( $\sim 44 \mu\text{m}$ ), was used as a diffusion source. The powder was placed on the Fe–1wt%Si specimen and was heated to 1100 °C for 2 h, held for 5 min, cooled to 950 °C for 2 h under flowing  $\text{H}_2$ , and then cooled in the furnace to room temperature as shown in Fig. 5.2. Then, to enhance diffusion



bonding kinetic, the holding time was increased from 5 min to 24 h where the other condition was the same with condition of Fig. 5.2. The bonding pressure is one of the major factors to enhance bonding between materials. To confirm the effect of bonding pressure, Si powders are placed on the Fe–1wt%Si specimen and are covered with Al<sub>2</sub>O<sub>3</sub> plate of 1.75g as shown in Fig. 5.3.

Si diffusion was induced using Hot Wire Chemical Vapor Devosition(HWCVD), which could easily control using gas flow control. Specimen temperature was controlled by a tungsten wire temperature with controller. Specimens were diffused under 1150 °C, 1050 °C, and 950 °C, and the diffusion was carried out for 30 min under various gas mixing conditions.

To investigate the texture evolution after the heat treatment, the specimen surface was polished less than 100 μm thickness to the final stage of colloidal silica (OP–s, 0.04 μm) and analyzed by electron back–scattered diffraction (EBSD, EDAX/Hikari) attached to a field emission scanning electron microscope (FESEM, SU5000, HITACHI). The EDAX/TSL software was used to analyze the orientation relationship. The components of specimens were investigated by energy dispersive spectrometry (EDS, EDAX/Hikari).

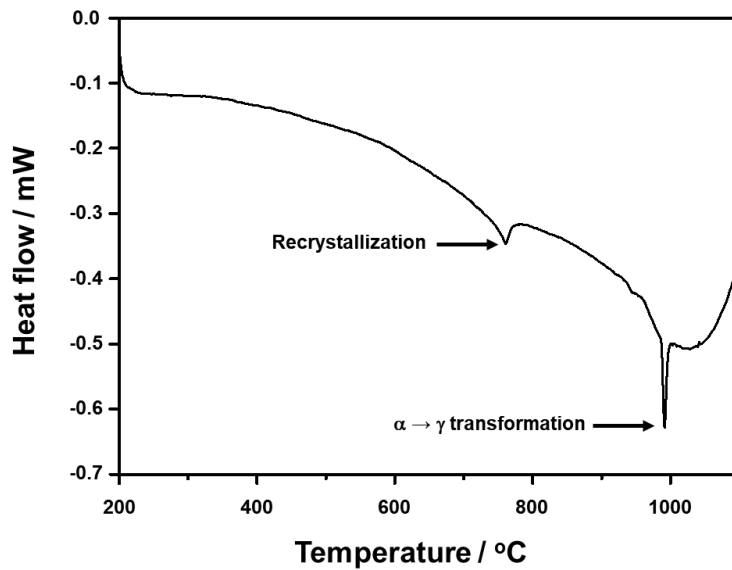


Fig. 5.1 DSC profile of the Fe-1wt%Si specimen measured during heating.

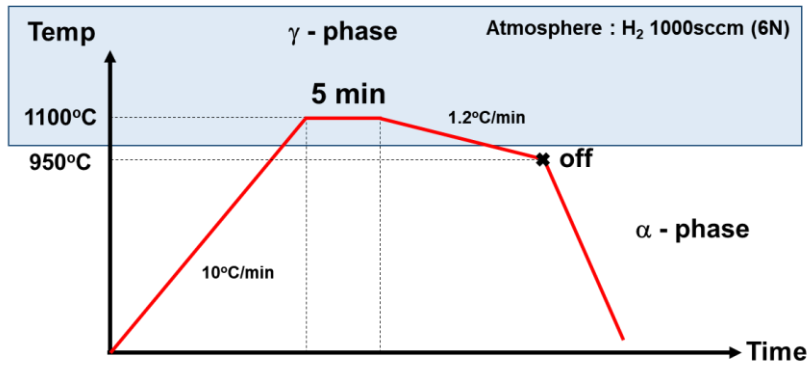


Fig. 5.2 Annealing condition for the  $\gamma \rightarrow \alpha$  phase transformation with commercially pure Si powder.

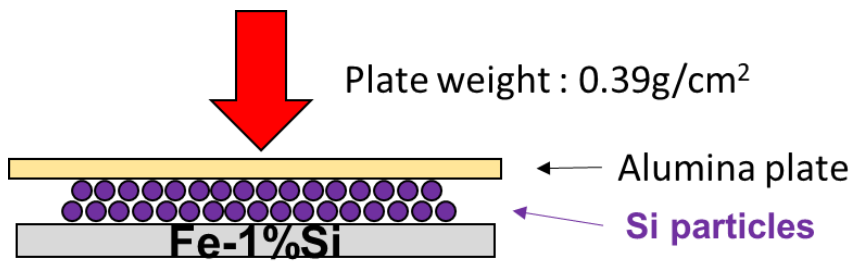


Fig. 5.3 Schematic image of heat treatment condition to enhance the bonding pressure.

### 5.3. Diffusion induced by B-doped Si wafer

Fig. 5.4 and Fig. 5.5 show schematics and photo images of before and after under the Si diffusion annealing condition. A Si wafer was placed on the Fe-1wt%Si specimen, which was in contact with each other as shown in Fig. 5.4 left. After annealing process, the surface morphology of specimen, which was in contact with Si wafer area, was changed because of the Si diffusion, and remained Si wafer was broken away as shown in schematic of Fig. 5.4 right. Fig. 5.5 shows the before and after photo images that of the experiment.

Fig. 5.6a and c shows the inverse pole figure (IPF) map and the orientation distribution function (ODF) sectioned at  $\varphi_2 = 45^\circ$  for the Fe-1wt%Si specimen heat treated without physical contact under 1100 °C holding for 5min with the slow cooling condition. Percentages of  $\{100\}$  and  $\{111\}$  were 14.2% and 11.9%, respectively, which were determined using the criteria of  $\{100\} \pm 15^\circ$ . Fig. 5.6b and d shows the IPF map and the ODF for the Fe-1wt%Si specimen heat treated under the physical contact with B-doped Si, where the other condition was the same with Fig. 5.6a. Percentages of  $\{100\}$  and  $\{111\}$  were 81.9% and 0.0%, respectively. Fig. 5.7a and c shows the IPF map and the ODF for

the Fe-1wt%Si specimen heat treated under the physical contact with B-doped Si at 1050 °C holding for 5 min with the slow cooling condition. Percentages of {100} and {111} were 67.1% and 15.5%, respectively. Fig. 5.7b and d shows the IPF map and the ODF for the Fe-1wt%Si specimen heat treated under the physical contact with B-doped Si at 1000 °C holding for 5min with the slow cooling condition. Percentages of {100} and {111} were 0.2% and 98.3%, respectively. The average grain sizes of Fig. 5.6 a, Fig. 5.6b, Fig. 5.7a and Fig. 5.7b were 193  $\mu\text{m}$ , 446  $\mu\text{m}$ , 311  $\mu\text{m}$  and 123  $\mu\text{m}$ , respectively, which was determined by converting the grain area into the diameter using an image analyzer software (EDAX/TSL software).

The specimen without physical contact with Si wafer under 1100 °C holding for 5 min with the slow cooling condition has weak texture which is close to random, the max intensity of ODF was 4.058 as shown in Fig. 5.6c. However, in case of the specimen which is in contact with Si wafer at 1100 °C holding for 5 min with the slow cooling condition, the intensity lines of  $\varphi_2$  section have uniform distribution, which means that a strong cube-on-face texture was evolved. The max intensity of ODF was 39.485 as shown in Fig. 5.6d. The weight percentage of the Si content measured by XRF inspector was 10.98%, which indicate that the Si

was diffused into the Fe-1wt%Si. The specimen which is in contact with Si wafer at 1050 °C holding for 5 min has relatively low percentage of {100} but the {111} was slightly increased. The weight percentage of the Si content in this condition was 11.10%. In case of the specimen in contact with Si wafer at 1000 °C holding for 5 min, totally different  $\gamma$  fiber texture was evolved. The weight percentage of the Si content in this condition was 0.63%, which means that Si diffusion was not progressed less than 1000 °C.

Then, how such a strong cube-on-face texture was evolved? The chapter 2 shows that physical contact with the dissimilar material can induce strong cube-on-face texture during  $\gamma \rightarrow \alpha$  phase transformation. In case of the chapter 2, Fe-1wt%Si specimen was sandwiched  $\text{Al}_2\text{O}_3$  pates, and  $\gamma \rightarrow \alpha$  phase transformation was progressed under the same condition of Fig. 5.6a. During  $\gamma \rightarrow \alpha$  annealing process, the tensile frictional stress was formed on the specimen surface because of the difference in thermal expansion coefficient. The tensile frictional stress on the specimen surface could affect the nucleation barrier during cooling, which reduce nucleation barrier on the surface and lead to evolution of strong {100} <0vw> texture. Similar results could be acquired by contact with quartz and tungsten materials.

Tomida et al. [13, 28, 30, 31] also made a cube-on-face

texture in a way other different such as a two stage annealing process. Fe-3wt%Si-1wt%Mn-0.5wt%C was used as a starting material. Heat treatment was conducted under the vacuum atmosphere higher than  $10^{-3}$  Pa for removing manganese. If the manganese could remove under the  $\gamma$  phase region, the phase would be transformed to  $\alpha$  phase because the manganese content act as  $\gamma$  phase stabilizer, the transformed  $\alpha$  phase would be an  $\langle 100 \rangle$  direction. Then decarburization process was conducted to induce inward growth. This result experimentally shows that the surface nucleation would be favor to the direction of  $\langle 100 \rangle$ . Both results have a common feature, the surface nucleation is critical for the formation of dominant  $\langle 100 \rangle$  direction.

Based on pervious discussion, a new concept was devised to evolve strong  $\{100\}\langle 0vw \rangle$  texture as shown in Fig. 5.4. If any components, which would be the  $\alpha$  phase stabilizer, could be diffused into Fe-1wt%Si specimen during  $\gamma$  phase, the diffused surface would take place the phase transformation to the  $\alpha$ , which orientation would be  $\{100\}\langle 0vw \rangle$ . From the weight percentage of Si in Fig. 5.7b, this indicate that the Si diffusion was not performed until 1000 °C. However, the Si content was diffused into the specimen under 1050 °C, and this temperature can be confirmed as a  $\gamma$  phase from the DSC data in Fig. 5.1. This result indicate that the



Si diffusion was performed under  $\gamma$  phase, which leads to  $\gamma \rightarrow \alpha$  phase transformation. From the former explanations, the surface nucleation induced by Si diffusion also has the preferred orientation of  $\{100\}\langle 0vw \rangle$ .

To understand the effect of Si diffusion more systemically, experiments were conducted under increasing the holding time of the specimen. Fig. 5.8 shows photo images of Si diffused specimens according to increasing the holding time. The Si diffused area can be easily distinguished, and as the holding time increases, the mass difference increased. Under the conditions of Fig. 5.8e and f, the diffusion and non-diffusion region were separated and fall off due to the difference in thermal expansion coefficient, which seems to be cut with a knife.

Fig. 5.9a and d shows the inverse pole figure (IPF) map and the orientation distribution function (ODF) sectioned at  $\varphi_2 = 45^\circ$ , respectively, for the Fe-1wt%Si specimen with Si diffused at 1100 °C holding for 2 min with the in and out condition. Percentages of  $\{100\}\langle 0vw \rangle$  and  $\{111\}\langle uvw \rangle$  were 77.9% and 0.5%, respectively. Fig. 5.9b and e shows the IPF map and the ODF, respectively, for the Fe-1wt%Si specimen with Si diffused at 1100 °C holding for 3.75 min with the in and out condition. Percentages of  $\{100\}\langle 0vw \rangle$  and  $\{111\}\langle uvw \rangle$  were 58.8% and 0.5%, respectively. Fig. 5.9c and

f shows the IPF map and the ODF, respectively, for the Fe-1wt%Si specimen with Si diffused at 1100 °C holding for 7.5 min with the in and out condition. Percentages of  $\{100\}\langle 0vw \rangle$  and  $\{111\}\langle uvw \rangle$  were 86.9% and 0%, respectively. The average grain sizes of Fig. 5.9a, b and c were 107  $\mu\text{m}$ , 147  $\mu\text{m}$  and 230  $\mu\text{m}$ , respectively. Fig. 5.10a and d shows the IPF map and the ODF, respectively, for the Fe-1wt%Si specimen with Si diffused at 1100 °C holding for 15 min with the in and out condition. Percentages of  $\{100\}\langle 0vw \rangle$  and  $\{111\}\langle uvw \rangle$  were 55.9% and 0.3%, respectively. Fig. 5.10b and e shows the IPF map and the ODF, respectively, for the Fe-1wt%Si specimen with Si diffused at 1100 °C holding for 30 min with the in and out condition. Percentages of  $\{100\}\langle 0vw \rangle$  and  $\{111\}\langle uvw \rangle$  were 63.7% and 0%, respectively. Fig. 5.10c and f shows the IPF map and the ODF, respectively, for the Fe-1wt%Si specimen with Si diffused at 1100 °C holding for 60 min with the in and out condition. Percentages of  $\{100\}\langle 0vw \rangle$  and  $\{111\}\langle uvw \rangle$  were 74.6% and 0%, respectively. The average grain sizes of Fig. 5.10a, b and c were 274  $\mu\text{m}$ , 352  $\mu\text{m}$  and 367  $\mu\text{m}$ , respectively.

Fig. 5.9 and Fig. 5.10 show that all the Si diffused specimens have strong  $\{100\}\langle 0vw \rangle$  texture, percentages of the other orientations were close to zero. The orientation distribution of all the samples has existed near the cube fiber and other orientations

were negligibly small. As the holding time increases, the average grain size increases, however, the grain size could not affect the  $\{100\}\langle 0vw \rangle$  evolution. This aspect is shown in Fig. 5.11 and Fig. 5.12, where percentages of  $\{100\}\langle 0vw \rangle$  was distributed from 55.9% to 86.9%, irrespective of the holding time at 1100 °C. However, percentages of Si content were influenced by increased holding time, the weight percentages of Si were, respectively, 9.38wt%, 9.86wt%, 10.22wt%, 10.25wt%, 11.48wt%, and 11.96wt%.

Fig. 5.13 and Fig. 5.14 show the IPF maps of cross section for the Fe-1wt%Si specimen with increase Si diffusion time. The Si diffusion depth of each specimen from surface to bulk was, respectively, 109  $\mu\text{m}$ , 161  $\mu\text{m}$ , 288  $\mu\text{m}$ , 381  $\mu\text{m}$ , 457  $\mu\text{m}$ , and 473  $\mu\text{m}$ . In case of the short time diffusion such as Fig. 5.13a, the diffusion depth was relatively low, but the orientation has a strong  $\{100\}\langle 0vw \rangle$  as shown in Fig. 5.9a and d, this result indicate that the surface nucleation induced by phase transformation with Si diffusion affects the evolution of  $\{100\}\langle 0vw \rangle$  texture and the  $\{100\}\langle 0vw \rangle$  grow into the bulk by the Si diffusion from the surface.

Fig. 5.15 and Fig. 5.16 show the line EDS analysis of cross section for the Fe-1wt%Si specimen with increased holding time. Both diffusion and non-diffusion area were separated as shown in Fig. 5.15 and Fig. 5.16a. This result indicate that the nucleated

orientation of  $\{100\}\langle 0vw \rangle$  was grow from contact with Si wafer surface to without contact surface of bottom.

Fig. 5.17 shows the EDS mapping images of the upper side area of the specimen after Si diffusion is complete. There exist a total of three layers and have different composition depending on the Si content. The first layer of (a) is Fe-Si with a composition of Fe-27.1wt%Si, the second layer of (b) is Fe<sub>2</sub>-Si (Fe-18wt%Si), and the third layer of (c) is ferrite with a composition of Fe-12wt%Si. Fig. 5.18 shows the schematic of the cross sectional image after Si diffusion is complete. The Fe-Si layer exists with voids and its thickness is about 20 μm and there is no voids in the second layer of Fe<sub>2</sub>-Si and its thickness is about 20 μm. In case of the third layer, there exists a void layer at the bottom surface. The result of the two voids layer formation in one specimen can be considered very specific case.

Then why such a specific result was happened? It is well known that when the mobility of one element is much higher than the other element in a phase boundary, voids would be formed because enough site are not available. Therefore, the results can be predicted by comparing the diffusion rates. The early stage of the Si diffusion during heat treatment at 1100 °C, α phase was formed between the Si wafer and Fe-1wtSi specimen, which has Fe-

12wt%Si composition. The Fe self-diffusivity of  $\gamma$  phase at 1100 °C is  $4.18 \times 10^{-15} \text{m}^2 \text{m}^{-1}$  and Si self-diffusivity at 1100 °C is  $1.21 \times 10^{-19} \text{m}^2 \text{m}^{-1}$ . Fe self-diffusivity of  $\alpha$  phase in  $\text{Fe}_{76}\text{-Si}_{24}$  at 1100 °C is  $1.27 \times 10^{-10} \text{m}^2 \text{m}^{-1}$  and Si self-diffusivity of  $\alpha$  phase in  $\text{Fe}_{76}\text{-Si}_{24}$  at 1100 °C is  $2.56 \times 10^{-13} \text{m}^2 \text{m}^{-1}$ . Comparing the Fe self-diffusivity between  $\alpha$  phase of  $\text{Fe}_{76}\text{-Si}_{24}$  and  $\gamma$  phase of Fe at 1100 °C,  $\alpha$  phase of  $\text{Fe}_{76}\text{-Si}_{24}$  is much higher than  $\gamma$  phase which could make voids at  $\alpha$  phase of  $\text{Fe}_{76}\text{-Si}_{24}$  and  $\gamma$  phase interface. In case of the Si self-diffusivity,  $\alpha$  phase of  $\text{Fe}_{76}\text{-Si}_{24}$  is much higher than Si which could also make voids at  $\alpha$  phase of  $\text{Fe}_{76}\text{-Si}_{24}$  and Si wafer interface. However, in case of the upper side, voids exist on Fe-Si layer, not Si- $\alpha$  interface. The previous result can be interpreted experimentally.

Fig. 5.19 and Fig. 5.20 show EDS mapping images of the upper side area of the specimen according to increase holding time at 1100 °C in Fe-1wt%Si contact with B-doped Si wafer. Fig. 5.19a shows the early stage of Si diffusion at 1100 °C holding for 2 min. Voids were formed at the interface between the  $\alpha$  and Si, the  $\alpha$  on the voids layer was surrounded by a Fe-Si. Considering Fe-Si phase diagram for these results, it can be expected that the Fe-Si was formed after  $\alpha$  phase is formed. As shown in Fig. 5.19 b and c, Fe-Si grows in the void layer as holding time increases. In the Fig.

5.16 a and b, The Si diffusion in the specimen thickness direction was finished between 15 min and 30 min.  $\text{Fe}_2\text{-Si}$  can't be observed at the interface between Fe-Si and  $\alpha$  under the 15 min condition, which is before the diffusion finish as shown in Fig. 5.20 a. However,  $\text{Fe}_2\text{-Si}$  was formed near the interface between Fe-Si and  $\alpha$  under the 30 min condition. These results mean that  $\text{Fe}_2\text{-Si}$  is precipitated near the interface between Fe-Si and  $\alpha$  after Si diffusion is completed. Then, as a diffusion time increases, it changes into a layer as shown in Fig. 5.20 c. These process can be shown in Fig 5.21.

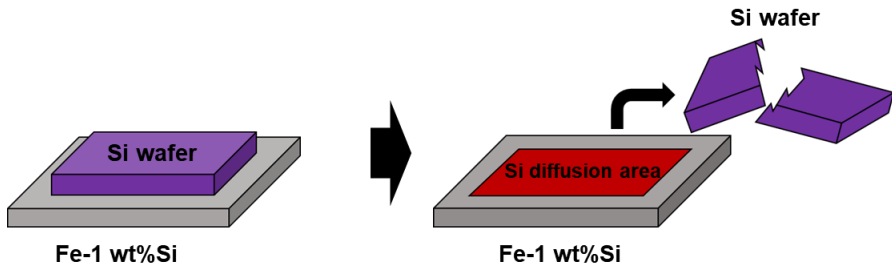


Fig. 5.4 Schematic of before & after Si diffusion image for Fe-1wt%Si specimen with B-doped Si wafer.

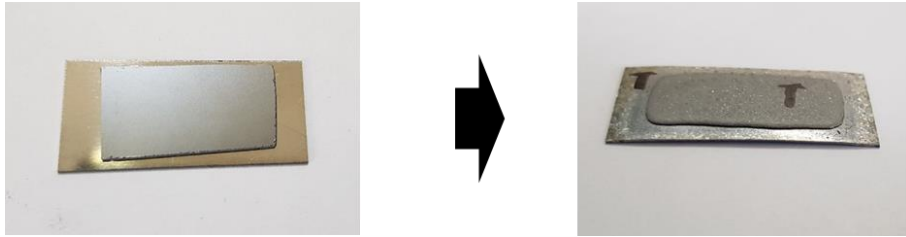


Fig. 5.5 Photo image of before & after Si diffusion for Fe-1wt%Si specimen with B-doped Si wafer.



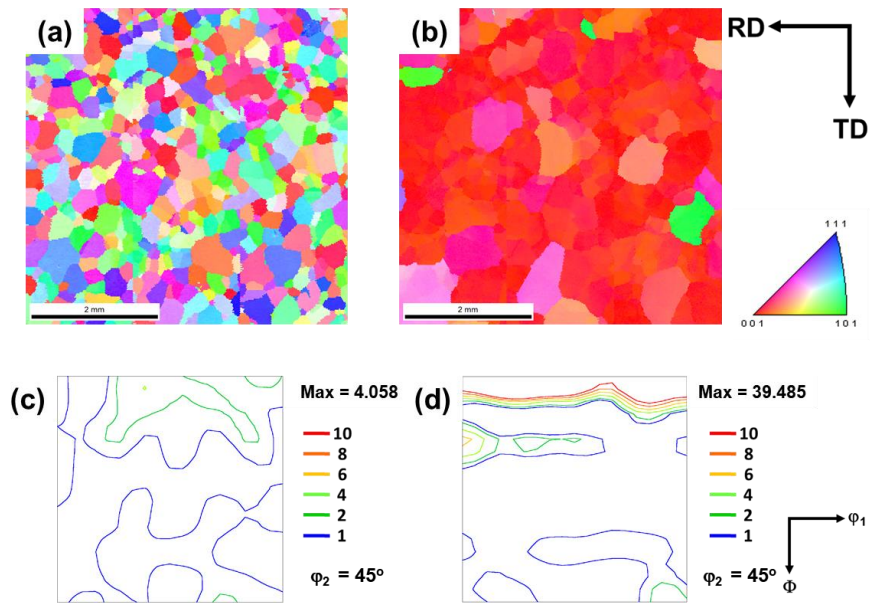


Fig. 5.6 EBSD IPF ND maps and 45° sections of ODF for the surface of specimens in Fe-1wt%Si annealed for 5 min with H<sub>2</sub> gas: (a), (c) at 1100 °C without contact and (b), (d) at 1100 °C in contacting with B-doped Si wafer.

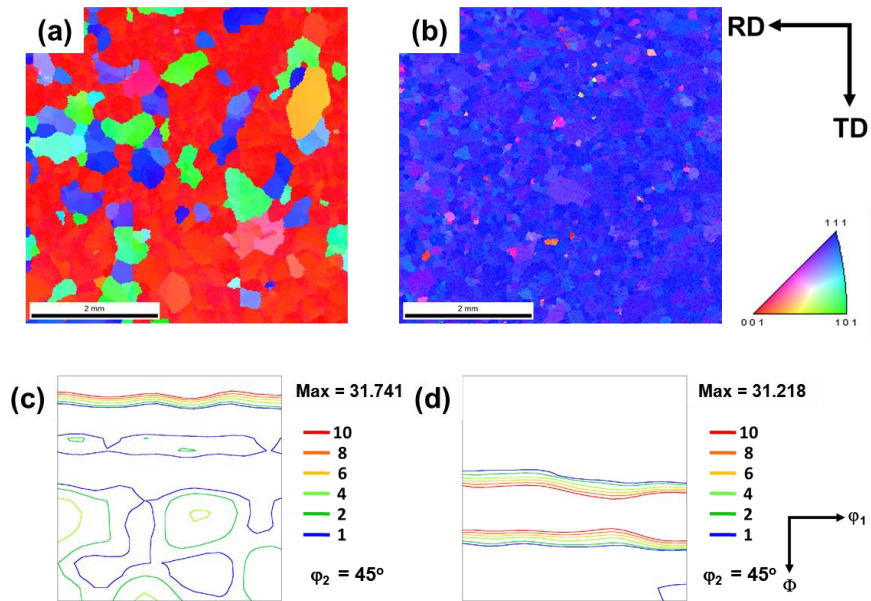


Fig. 5.7 EBSD IPF ND maps and  $45^\circ$  sections of ODF for the surface of specimens in Fe-1wt%Si annealed for 5 min with  $H_2$  gas: (a), (c) at 1050 °C in contacting with B-doped Si wafer and (b), (d) at 1000 °C in contacting with B-doped Si wafer.

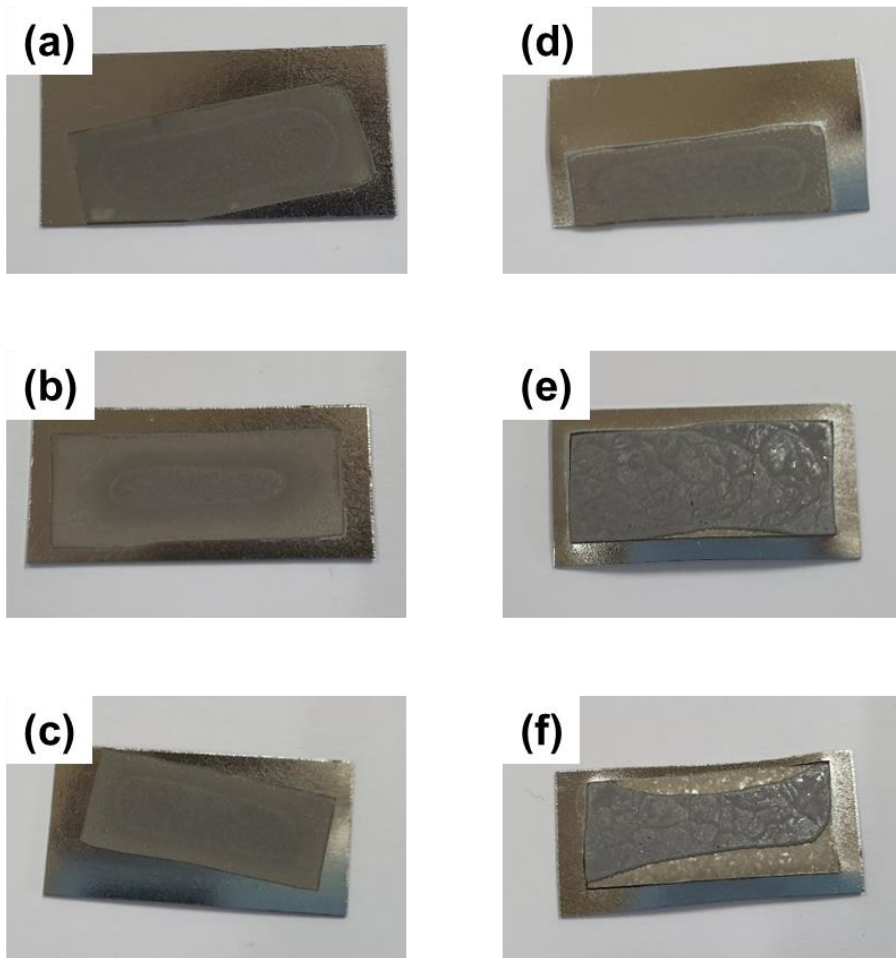


Fig. 5.8 Si diffused specimens according to increase holding time at 1100 °C : (a) 2 min, (b) 3.75 min, (c) 7.5 min, (d) 15 min (e) 30 min and (f) 60 min.

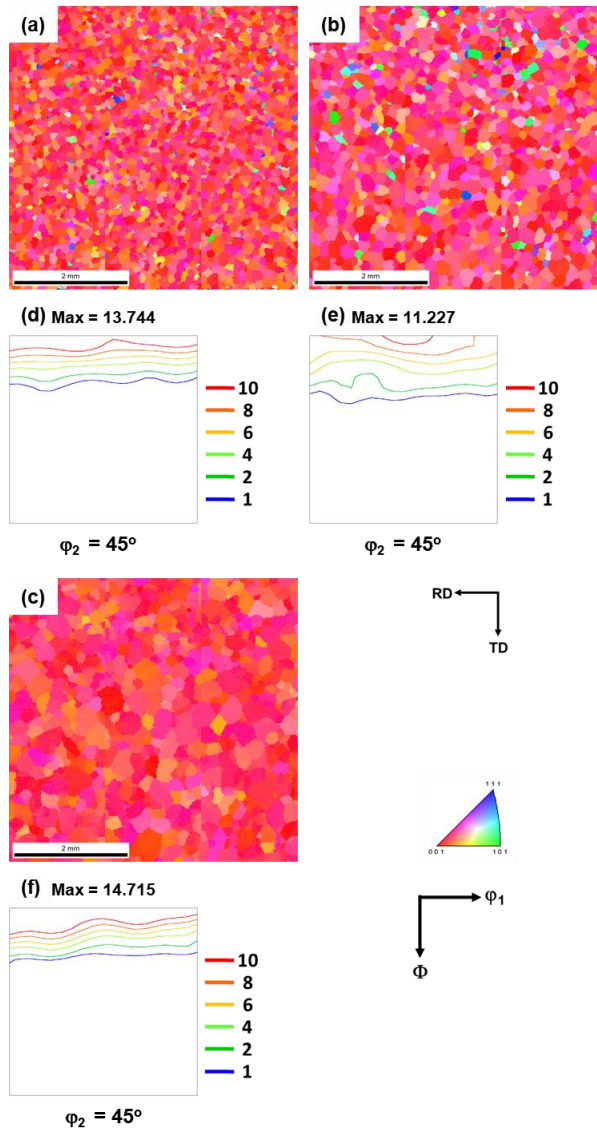


Fig. 5.9 EBSD IPF ND maps and 45° sections of ODF for the surface of Si diffused specimens according to increase holding time at 1100 °C in Fe–1wt%Si contact with B–doped Si wafer : (a), (d) 2 min (b), (e) 3.75 min and (d), (f) 7.5 min.

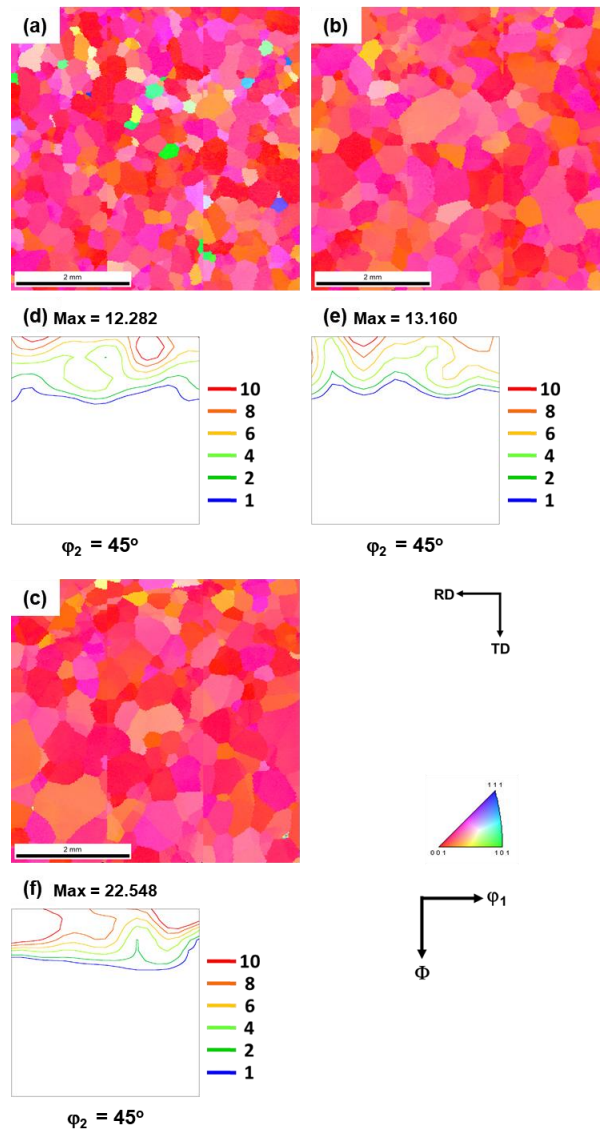


Fig. 5.10 EBSD IPF ND maps and 45° sections of ODF for the surface of Si diffused specimens according to increase holding time at 1100 °C in Fe-1wt%Si contact with B-doped Si wafer : (a), (d) 15 min (b), (e) 30 min and (d), (f) 60 min.

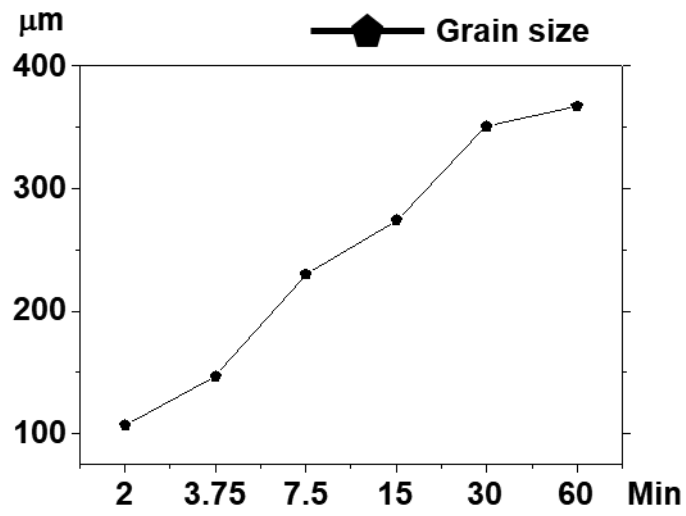


Fig. 5.11 Grain size distribution for Si diffused specimens with increased diffusion time at 1100 °C.

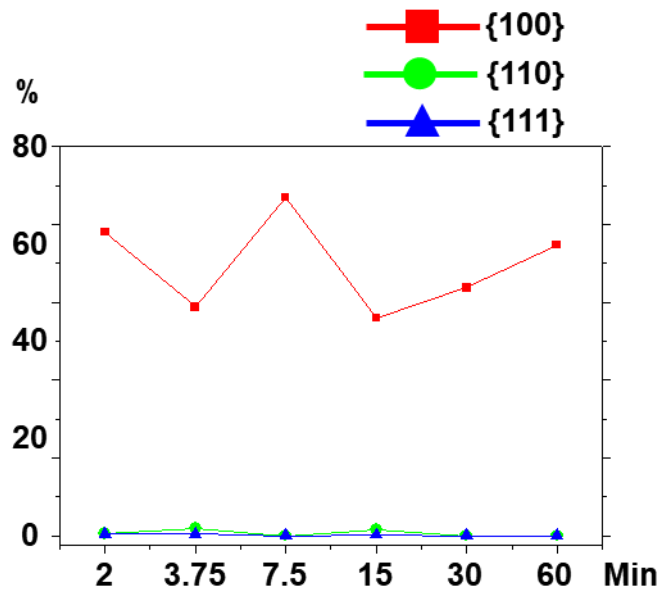


Fig. 5.12 Percentages of major orientations for Si diffused specimens with increased diffusion time at 1100 °C.

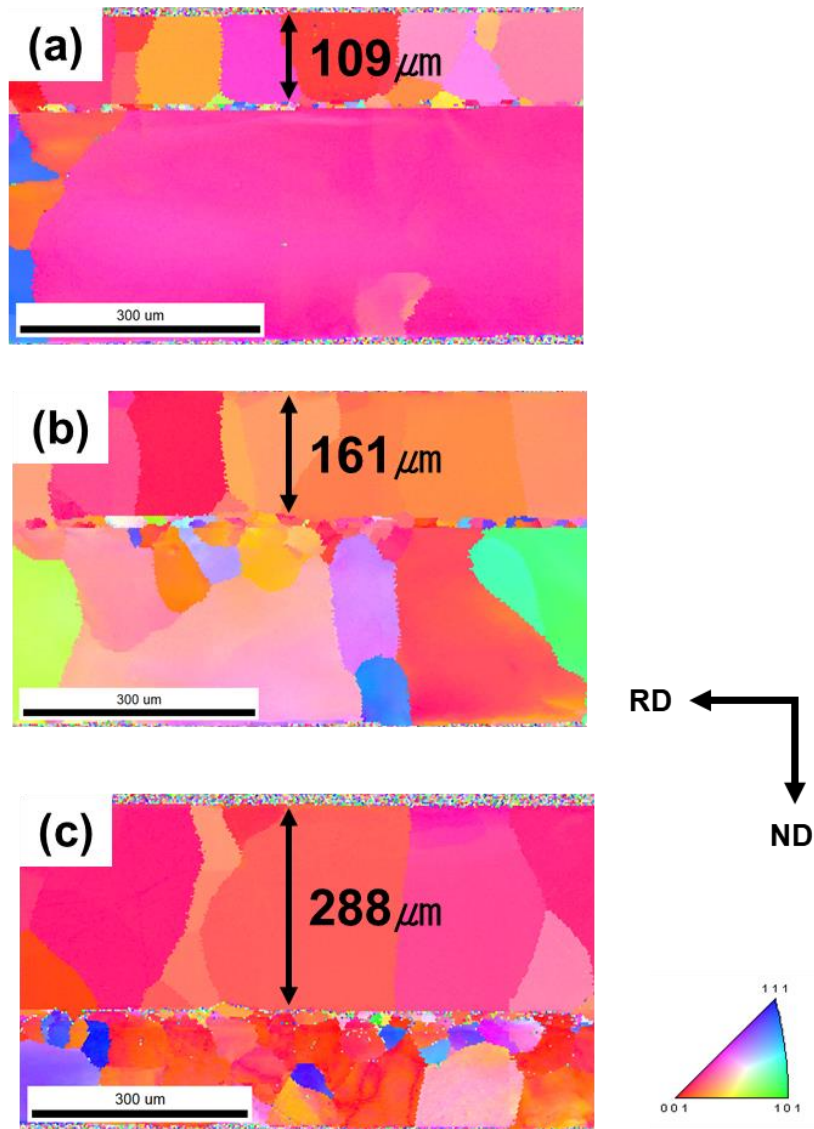


Fig. 5.13 EBSD IPF ND maps for the cross section of Si diffused specimens according to increase holding time at 1100 °C in Fe-1wt%Si contact with B-doped Si wafer : (a) 2 min, (b) 3.75 min sec and (c) 7.5 min, respectively.



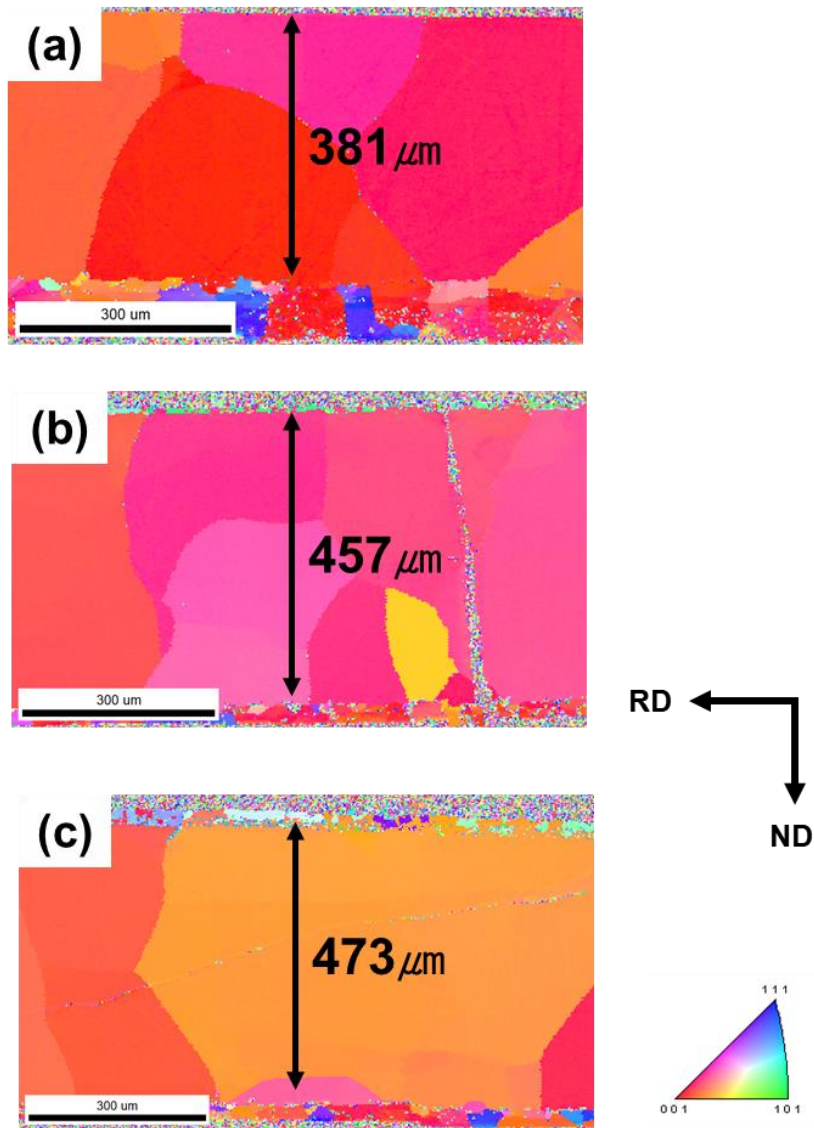


Fig. 5.14 EBSD IPF ND maps for the cross section of Si diffused specimens according to increase holding time at 1100 °C in Fe-1wt%Si contact with B-doped Si wafer : (a) 15 min, (b) 30 min sec and (c) 60 min, respectively.

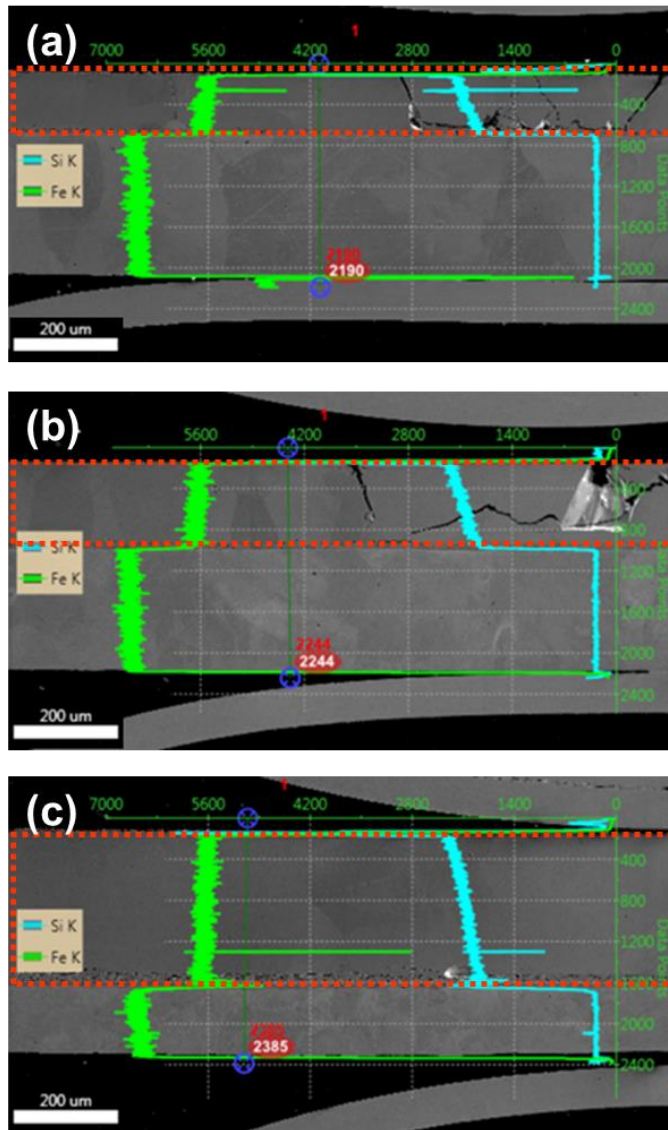


Fig. 5.15 Line EDS images for the cross section of Si diffused specimens according to increase holding time at 1100 °C in Fe-1wt%Si contact with B-doped Si wafer : (a) 2 min, (b) 3.75 min and (c) 7.5 min, respectively.

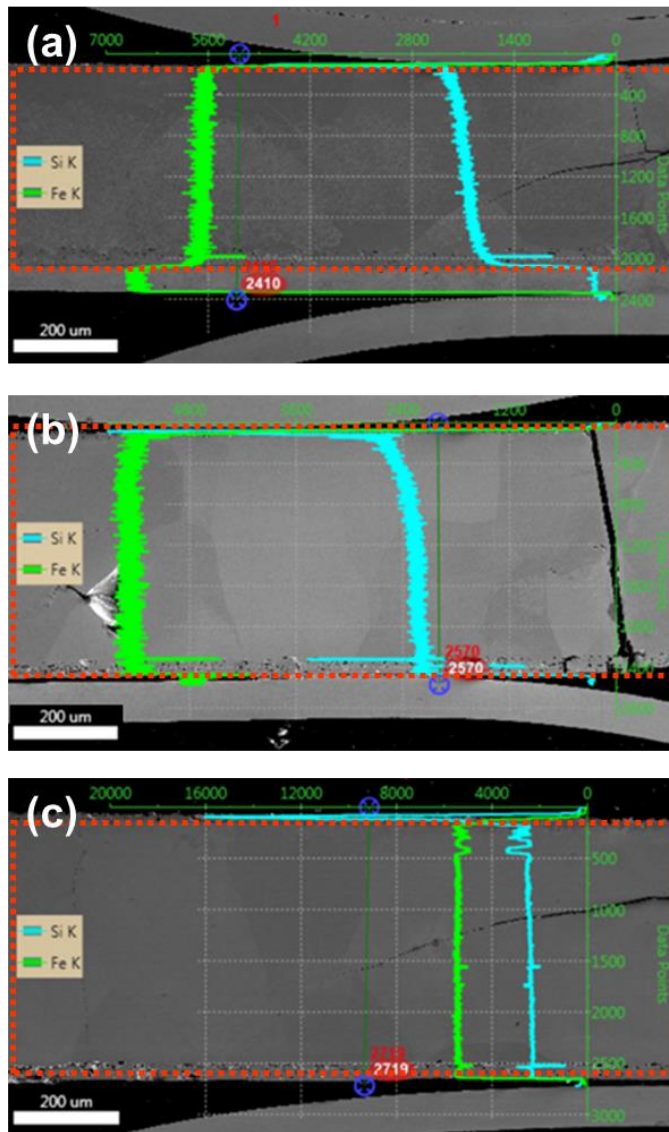


Fig. 5.16 Line EDS images for the cross section of Si diffused specimens according to increase holding time at 1100 °C in Fe–1wt%Si contact with B–doped Si wafer : (a) 15 min, (b) 30 min and (c) 60 min, respectively.

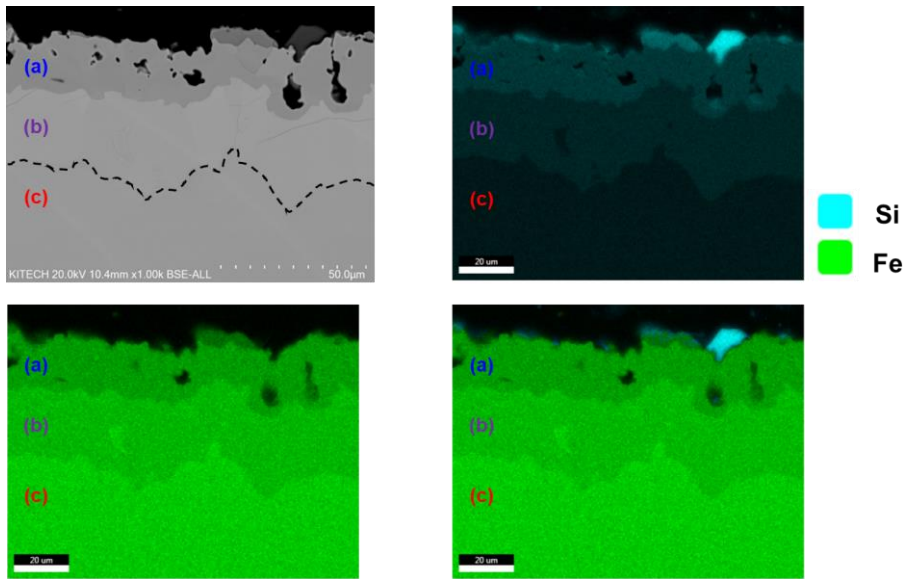


Fig. 5.17 EDS mapping images of the upper side area of the specimen after Si diffusion : (a) Fe–Si layer, (b)  $\text{Fe}_2\text{-Si}$  and (c) Ferrite, respectively.

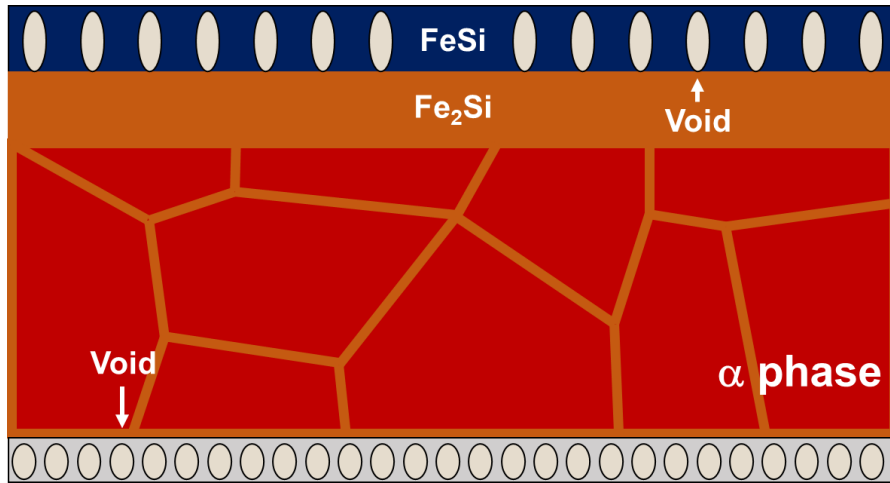


Fig. 5.18 Schematic of the cross sectional image after completion of Si diffusion.

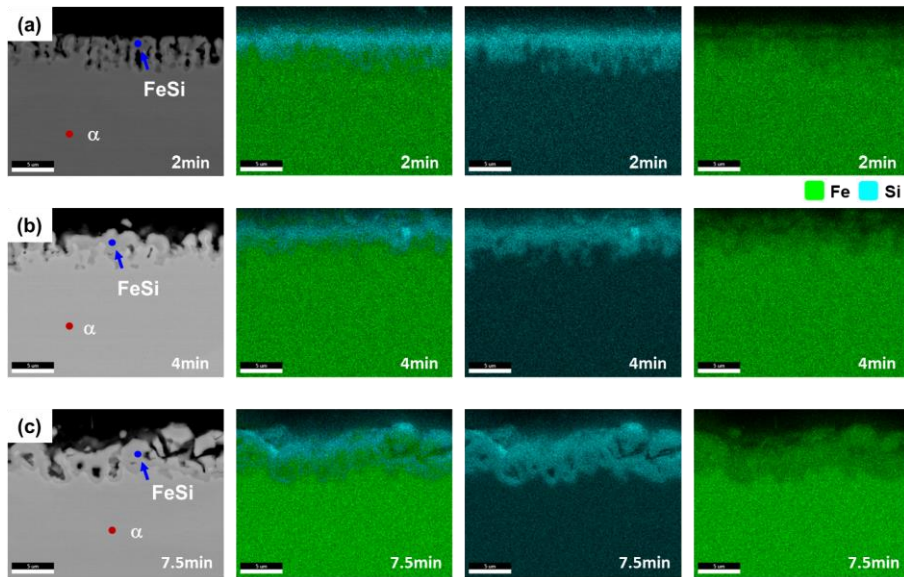


Fig. 5.19 EDS mapping images of the upper side area of the specimen according to increase holding time at 1100 °C in Fe-1wt%Si contact with B-doped Si wafer : (a) 2 min, (b) 3.75 min and (c) 7.5 min, respectively.

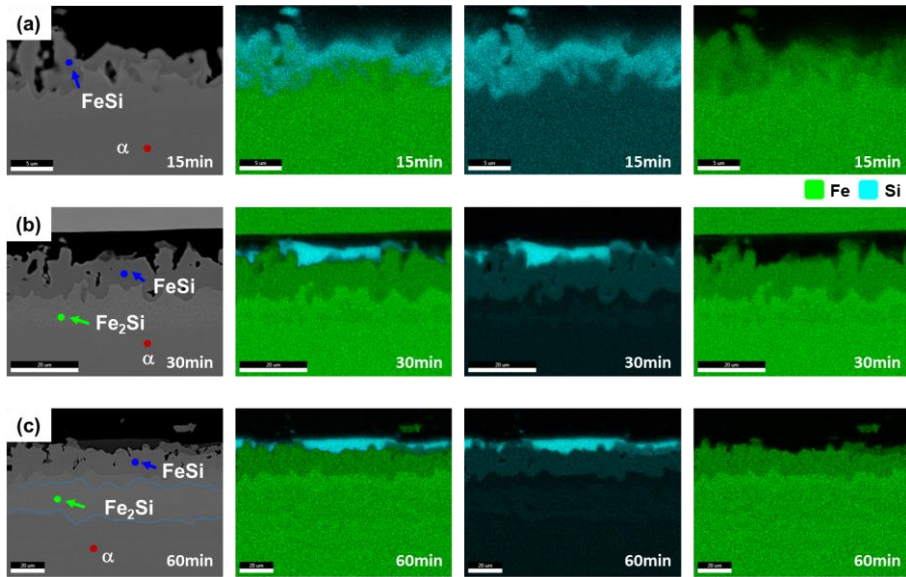


Fig. 5.20 EDS mapping images of the upper side area of the specimen according to increase holding time at 1100 °C in Fe–1wt%Si contact with B–doped Si wafer : (a) 15 min, (b) 30 min and (c) 60 min, respectively.



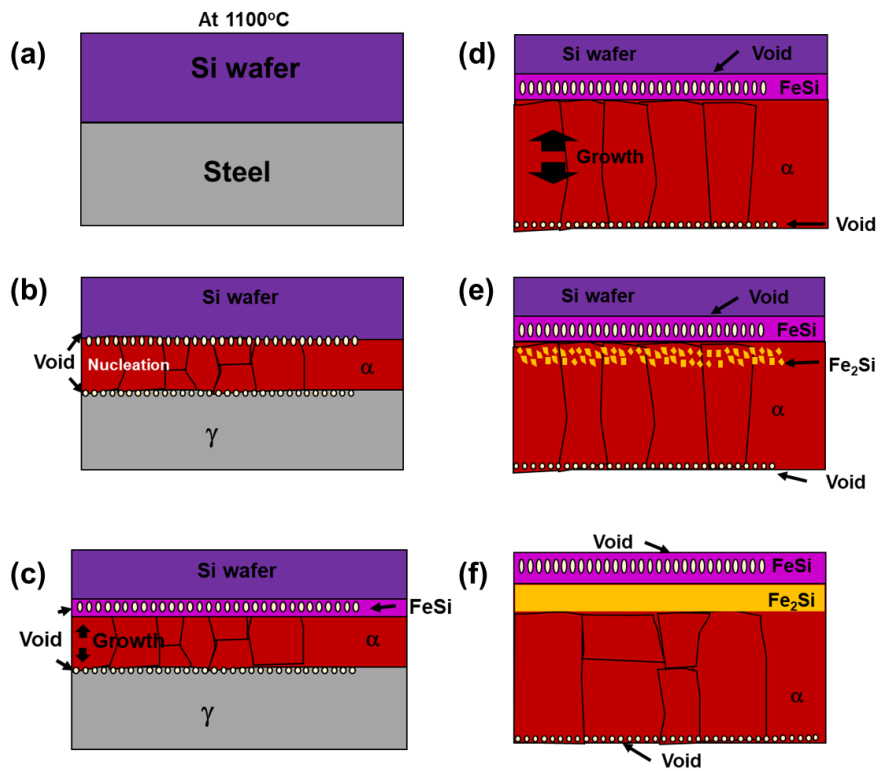


Fig. 5.21 Schematics of alloying layers and voids formation during Si diffusion process.



## 5.4. Diffusion induced by Si powder

Fig. 5.22a and b shows the inverse pole figure (IPF) map and the orientation distribution function (ODF) sectioned at  $\varphi_2 = 45^\circ$  for the Fe-1wt%Si specimen heat treated physical contact with Si powders under 1100 °C holding for 5min, cooled to 950 °C for 120 min and cooled to room temperature in the furnace. Percentages of  $\{100\}\langle 0vw \rangle$  and  $\{111\}\langle uvw \rangle$  were 0.6% and 85.0%, respectively, which were determined using the criteria of  $\{100\}\langle 0vw \rangle \pm 15^\circ$ . Fig. 5.23a and b shows the IPF ND map and the ODF for the Fe-2wt%Si-1wt%Ni specimen heat treated under 1100 °C holding for 12 h, where the other condition was the same with Fig. 5.22. Percentages of  $\{100\}\langle 0vw \rangle$  and  $\{111\}\langle uvw \rangle$  were 0.1% and 97.4%, respectively. The average grain sizes of Fig. 5.22a and Fig. 5.23a were 92  $\mu\text{m}$  and 225  $\mu\text{m}$ , respectively, which were determined by converting the grain area into the diameter using an image analyzer software (EDAX/TSL software).

The weight percentage of Fig. 5.22 by EDS analysis is 0.92% which means that Si diffusion was not induced. There are three major parameters to induce diffusion process: (1) pressure, (2) temperature, (3) holding time. To make diffusion bonding between the specimen and powders, the holding time under 1100 °C was

increased from 5min to 12 h. Fig.5. 23 shows that the grain size increased to 225  $\mu\text{m}$  but strong  $\gamma$  fiber texture was developed. The weight percentage of Fig. 5.23 is 0.96% which means that a diffusion was not induced although the holding time increased to 12 h.

To confirm the effect of a bonding pressure, the  $\text{Al}_2\text{O}_3$  plate was placed on the powders to add a pressure between the specimen and powders, and annealing process was conducted under the same with Fig. 5.22. Fig. 5.24 shows the cross sectional SEM image after the annealing process under the specimen pressed by  $\text{Al}_2\text{O}_3$  plate. Large amount of voids was observed. Weight percentages of Si were 15.51%, 15.40% and 15.58%, respectively, which means that the Si diffusion underwent by an increasing bonding pressure. Fig.5. 25 shows the inverse pole figure (IPF) map for the Fe-1wt%Si specimen. Percentages of  $\{100\}\langle 0vw\rangle$ ,  $\{110\}\langle uvw\rangle$  and  $\{111\}\langle uvw\rangle$  were 12.5%, 19.5 and 11.5%, respectively. This result shows that a successful diffusion process underwent but a random texture was developed instead of cube-on-face texture. The reason for this texture development can be interpreted as whether the phase transformation was progressed or not. It is expected that the Si diffusion was started from a  $\alpha$  phase stable temperature, which leads to the random texture development.

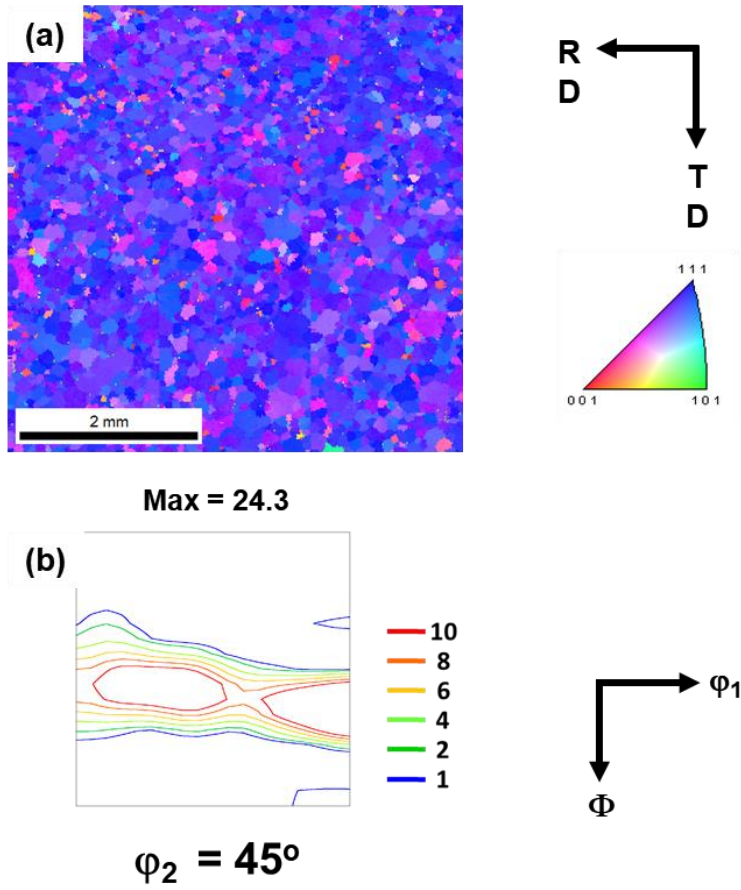


Fig. 5.22 EBSD IPF ND maps and  $45^\circ$  sections of ODF for the surface of Si diffused specimens at  $1100^\circ\text{C}$  holding for 5 min in Fe-1wt%Si contact with Si powders : (a) IPF map and (b) ODF.

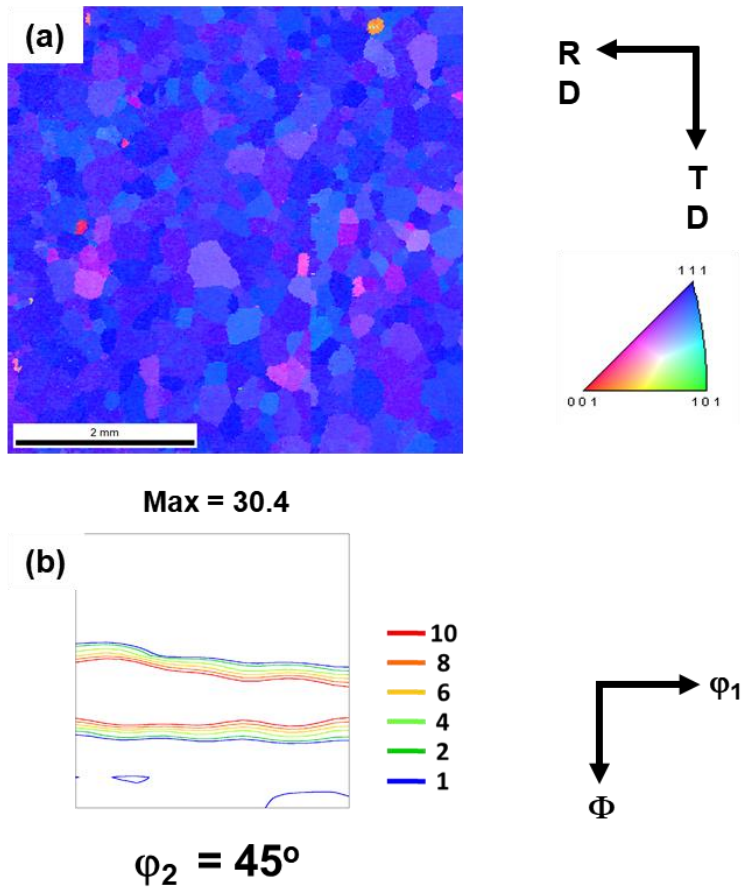


Fig. 5.23 EBSD IPF ND maps and  $45^\circ$  sections of ODF for the surface of Si diffused specimens at  $1100^\circ\text{C}$  holding for 12 h in Fe–1wt%Si contact with Si powders : (a) IPF map and (b) ODF.

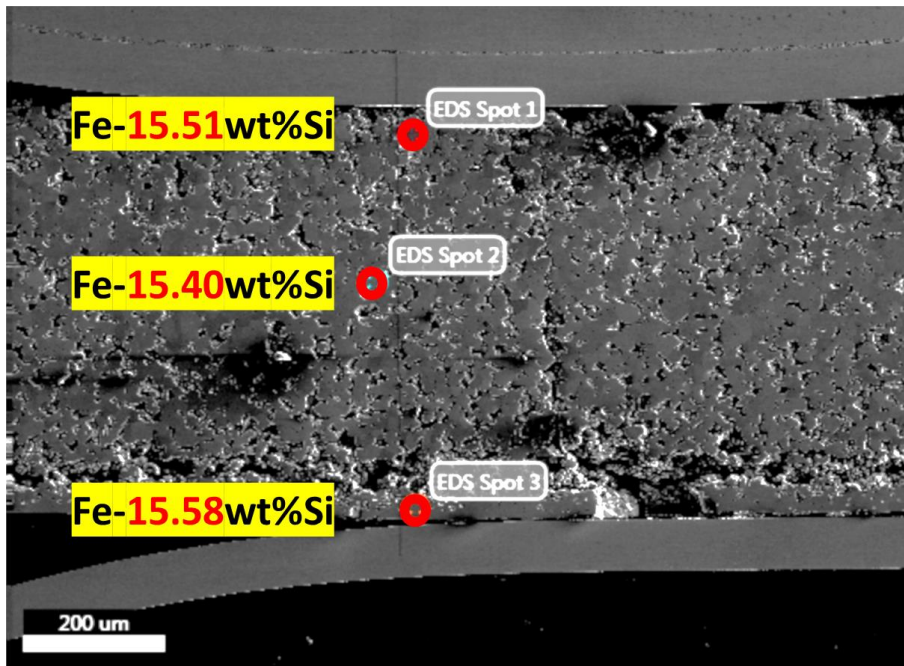


Fig. 5.24 SEM cross sectional image at 1100 °C holding for 5 min in Fe-1wt%Si pressed by Al<sub>2</sub>O<sub>3</sub> plate.

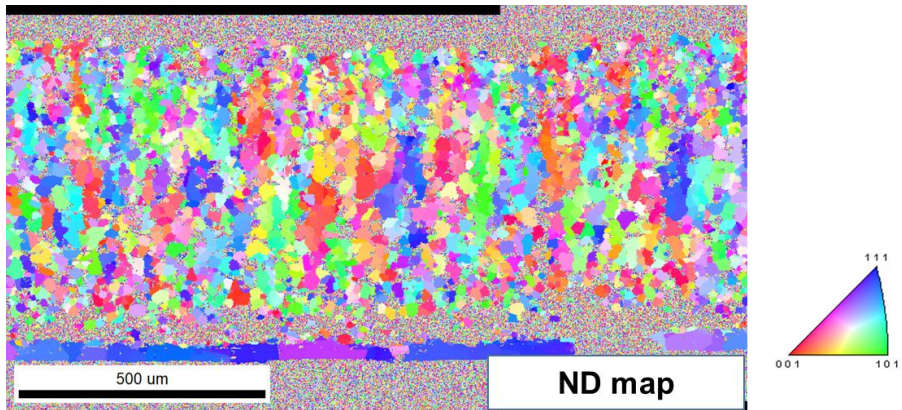


Fig. 5.25 EBSD IPF ND maps for the cross section of Si diffused specimens at 1100 °C in Fe-1wt%Si pressed by a Al<sub>2</sub>O<sub>3</sub> plate.

## Chapter 6. Conclusions

The tensile stress induced on the surface by the physical contact, which is generated by the difference in a thermal expansion coefficient between the specimen and the supporting plates, is suggested to affect the evolution of  $\{100\}\langle 0vw \rangle$  texture in Fe-1wt%Si. Cube-on-face texture was evolved under the physical contact with  $\text{Al}_2\text{O}_3$ , quartz and tungsten which thermal expansion coefficient is less than half of that of Fe whereas  $\{111\}\langle uvw \rangle$  texture was evolved under the physical contact with nickel which has similar thermal expansion coefficient of Fe.

The tensile stress induced by the creep deformation due to the self-load has a similar effect with the physical contact. Using the self-load method 88.0% of  $\{100\}\langle 0vw \rangle$  texture was developed in Fe-1wt%Si. This method was extended to Fe-2wt%Si-1wt%Ni composition resulting in 77.7% of  $\{100\}\langle 0vw \rangle$  texture by a self-load and a grain growth to enhance the probability of surface nucleation.

The stress effect is extended to uniaxial compressive stress for the development of cube-on-face texture. A compressive stress induced by a specimen placement affects a grain growth. The nucleation barrier was affected by a compressive stress which

increase nucleation barrier during  $\gamma \rightarrow \alpha$  phase transformation resulting in strong cube-on-face texture development by an increasing the probability of surface nucleation.

Three types of texture controlled specimens were prepared to confirm how the magnetic properties could be affected by a texture development with the same chemical composition of Fe-2wt%Si-1wt%Ni. The specimen with 78.4% of  $\{100\}\langle 0vw \rangle$ , and 3.2% of  $\{111\}\langle uvw \rangle$  produce the highest magnetic flux density of  $B_{50} = 1.75$  and the lowest iron loss of  $W_{15/50} = 2.19$ . The specimen with 0.7% of  $\{100\}\langle 0vw \rangle$ , and 81.3% of  $\{111\}\langle uvw \rangle$  produce the lowest magnetic flux density of  $B_{50} = 1.61$  and the highest iron loss of  $W_{15/50} = 2.50$ . Therefore, the magnetic properties strongly depend on the texture development

A new concept, which is  $\gamma \rightarrow \alpha$  phase transformation induced by the Si diffusion on the specimen surface, is proposed to evolve strong  $\{100\}\langle 0vw \rangle$  texture.  $\{100\}\langle 0vw \rangle$  of an  $\alpha$  nuclei can be formed on the specimen surface by a Si diffusion and be grown into the bulk as annealing time increased, which was experimentally confirmed. A strong  $\{100\}\langle 0vw \rangle$  texture of 86.9% was produced under the 7.5 min holding time of in and out condition.



# Bibliography

- [1] A.J. Moses, Energy efficient electrical steels: Magnetic performance prediction and optimization, *Scripta Materialia*, 67 (2012) 560–565.
- [2] T.-W. Na, H.-K. Park, C.-S. Park, J.-T. Park, N.-M. Hwang, Misorientation angle analysis near the growth front of abnormally growing grains in 5052 aluminum alloy, *Acta Materialia*, 115 (2016) 224–229.
- [3] H.-K. Park, J.-H. Kang, C.-S. Park, C.-H. Han, N.-M. Hwang, Pancake-shaped growth of abnormally-growing Goss grains in Fe-3%Si steel approached by solid-state wetting, *Materials Science and Engineering: A*, 528 (2011) 3228–3231.
- [4] K. Günther, G. Abbruzzese, S. Fortunati, G. Ligi, Recent Technology Developments in the Production of Grain-Oriented Electrical Steel, *steel research international*, 76 (2005) 413–421.
- [5] L. Zhang, P. Yang, J. Wang, W. Mao, Transformation of {100} texture induced by surface effect in ultra-low carbon electrical steel, *Journal of Materials Science*, 51 (2016) 8087–8097.
- [6] L. Cheng, N. Zhang, P. Yang, W.M. Mao, Retaining {100} texture from initial columnar grains in electrical steels, *Scripta Materialia*, 67 (2012) 899–902.
- [7] J.J. Sidor, K. Verbeken, E. Gomes, J. Schneider, P.R. Calvillo, L.A.I. Kestens, Through process texture evolution and magnetic properties of high Si non-oriented electrical steels, *Materials Characterization*, 71 (2012) 49–57.
- [8] S. Jin Kyung, K. Yang Moo, Magnetic properties of Fe and Fe-Si alloys with {100}  $\langle 0vw \rangle$  texture, *Journal of Applied Physics*, 113 (2013).
- [9] L. Xie, P. Yang, N. Zhang, C. Zong, D. Xia, W. Mao, Formation of {100} textured columnar grain structure in a non-oriented electrical steel by phase transformation, *Journal of Magnetism and Magnetic Materials*, 356 (2014) 1–4.
- [10] M. Sanjari, Y. He, E.J. Hilinski, S. Yue, L.A.I. Kestens, Development of the {113}  $\langle uvw \rangle$  texture during the annealing of a skew cold rolled non-oriented electrical steel, *Scripta Materialia*, 124 (2016) 179–183.
- [11] R. Liang, P. Yang, W. Mao, Cube texture evolution and magnetic properties of 6.5 wt% Si electrical steel fabricated by surface energy and three-stage rolling method, *Journal of Magnetism and Magnetic Materials*, 457 (2018) 38–45.
- [12] M. Mehdi, Y. He, E.J. Hilinski, A. Edrissy, Texture Evolution of a 2.8 wt% Si Non-Oriented Electrical Steel during Hot Band Annealing, *IOP Conference Series: Materials Science and Engineering*, 375 (2018).
- [13] T. Tomida, S. Uenoya, Cube oriented 3% Si-1% Mn soft magnetic steel sheets with fine grain structure, *IEEE transactions on magnetics*, 37 (2001) 2318–2320.
- [14] H.-T. Liu, H.-Z. Li, H.-L. Li, F. Gao, G.-H. Liu, Z.-H. Luo, F.-Q. Zhang, S.-L. Chen, G.-M. Cao, Z.-Y. Liu, G.-D. Wang, Effects of rolling temperature on microstructure, texture, formability and magnetic properties

in strip casting Fe-6.5 wt% Si non-oriented electrical steel, *Journal of Magnetism and Magnetic Materials*, 391 (2015) 65-74.

[15] K. Shoji, N. Misao, H. Tatsuhiko, Recent Progress of High Silicon Electrical Steel, *JFE GIHO*, (2015) 2-16.

[16] F. Kováč, M. Dzubinský, Y. Sidor, Columnar grain growth in non-oriented electrical steels, *Journal of Magnetism and Magnetic Materials*, 269 (2004) 333-340.

[17] I.V. Gervas'eva, V.A. Zimin, Textural and structural transformations in nonoriented electrical steel, *The Physics of Metals and Metallography*, 108 (2009) 455-465.

[18] H.-T. Liu, Z.-Y. Liu, Y. Sun, Y.-Q. Qiu, C.-G. Li, G.-M. Cao, B.-D. Hong, S.-H. Kim, G.-D. Wang, Formation of {001} <510> recrystallization texture and magnetic property in strip casting non-oriented electrical steel, *Materials Letters*, 81 (2012) 65-68.

[19] Y. Hu, V. Randle, T. Irons, Macrotexture and microtexture evolution in cold rolled non-oriented electrical steel sheets during annealing, *Materials Science and Technology*, 22 (2013) 1333-1337.

[20] M. Gallagher, A. Samimi, T.W. Krause, L.C. Clapham, R.R. Chromik, Local Magnetic Properties in Non-oriented Electrical Steel and Their Dependence on Magnetic Easy Axis and Misorientation Parameters, *Metallurgical and Materials Transactions A*, 46 (2015) 1262-1276.

[21] H.-T. Liu, J. Schneider, H.-L. Li, Y. Sun, F. Gao, H.-H. Lu, H.-Y. Song, L. Li, D.-Q. Geng, Z.-Y. Liu, G.-D. Wang, Fabrication of high permeability non-oriented electrical steels by increasing <001> recrystallization texture using compacted strip casting processes, *Journal of Magnetism and Magnetic Materials*, 374 (2015) 577-586.

[22] A. Stöcker, J. Schneider, T. Scholze, A. Franke, H. Hermann, R. Kawalla, Influence of cubic texture intensity of hot rolled ferritic non-oriented electrical steels on the microstructure and texture in the final processed material, *IOP Conference Series: Materials Science and Engineering*, 82 (2015).

[23] L. Xie, P. Yang, D. Xia, W. Mao, Microstructure and texture evolution in a non-oriented electrical steel during  $\gamma \rightarrow \alpha$  transformation under various atmosphere conditions, *Journal of Magnetism and Magnetic Materials*, 374 (2015) 655-662.

[24] K.-M. Kim, H.-K. Kim, J.Y. Park, J.S. Lee, S.G. Kim, N.J. Kim, B.-J. Lee, {100} texture evolution in bcc Fe sheets - Computational design and experiments, *Acta Materialia*, 106 (2016) 106-116.

[25] J. Schneider, A. Stöcker, A. Franke, R. Kawalla, Effects by the microstructure after hot and cold rolling on the texture and grain size after final annealing of ferritic non-oriented FeSi electrical steel, *AIP Advances*, 8 (2018).

[26] P. Yang, L. Zhang, J. Wang, W. Mao, Improvement of Texture and Magnetic Properties by Surface Effect Induced Transformation in Non-Oriented Fe-0.82Si-1.37Mn Steel Sheets, *steel research international*, 89 (2018).

[27] M.L. Kuo, D.J. Poxson, Y.S. Kim, F.W. Mont, J.K. Kim, E.F. Schubert, S.Y. Lin, Realization of a near-perfect antireflection coating for silicon solar

energy utilization, *Opt Lett*, 33 (2008) 2527–2529.

[28] T. Tomida, T. Tanaka, Development of (100) texture in silicon steel sheets by removal of manganese and decarburization, *ISIJ international*, 35 (1995) 548–556.

[29] H.-Z. Li, H.-T. Liu, Z.-Y. Liu, H.-H. Lu, H.-Y. Song, G.-D. Wang, Characterization of microstructure, texture and magnetic properties in twin-roll casting high silicon non-oriented electrical steel, *Materials Characterization*, 88 (2014) 1–6.

[30] T. Tomida, S. Uenoya, N. Sano, Fine-grained doubly oriented silicon steel sheets and mechanism of cube texture development, *Materials transactions*, 44 (2003) 1106–1115.

[31] T. Tomida, A new process to develop (100) texture in silicon steel sheets, *Journal of materials engineering performance* 5(1996) 316–322.

[32] J.K. Sung, D.N. Lee, D.H. Wang, Y.M. Koo, Efficient generation of cube-on-face crystallographic texture in iron and its alloys, *ISIJ international*, 51 (2011) 284–290.

[33] S.-B. Kwon, Y.-K. Ahn, Y.-K. Jeong, T.-Y. Kim, J.-T. Park, H.N. Han, N.-M. Hwang, Evolution of cube-on-face texture in Fe-1%Si steel induced by physical contact during the phase transformation from  $\gamma$  to  $\alpha$ , *Materials Characterization*, 165 (2020).

[34] N.H. Heo, K.H. Chai, J.G. Na, Correlation between interfacial segregation and surface-energy-induced selective grain growth in 3% silicon-iron alloy, *Acta Materialia*, 48 (2000) 2901–2910.

[35] S.-B. Kwon, Y.-K. Ahn, Y.-K. Jeong, T.-Y. Kim, J.-T. Park, H.N. Han, N.-M. Hwang, Evolution of cube-on-face texture in Fe-1%Si steel induced by physical contact during the phase transformation from  $\gamma$  to  $\alpha$ , *Materials Characterization*, (2020) 110380.

[36] Y.-K. Ahn, S.-B. Kwon, Y.-K. Jeong, J.-U. Cho, T.-Y. Kim, N.-M. Hwang, Fabrication of cube-on-face textured Fe-1wt%Si and Fe-2wt%Si-1wt%Ni electrical steel using surface nucleation during  $\gamma \rightarrow \alpha$  phase transformation, *Materials Characterization*, 170 (2020) 110724.

[37] P. Auerkari, *Mechanical and physical properties of engineering alumina ceramics*, 1996.

[38] D. Sastry, *The Metals Data Book by Alok Nayar*, *Bulletin of Materials Science*, 21 (1998) 105–105.

[39] H. Sunami, Y. Itoh, K. Sato, Stress and Thermal-Expansion Coefficient of Chemical-Vapor-Deposited Glass Films, *Journal of Applied Physics*, 41 (1970) 5115–5117.

[40] P.-L. Chen, I.-W. Chen, Grain Growth in CeO<sub>2</sub>: Dopant Effects, Defect Mechanism, and Solute Drag, *Journal of the American Ceramic Society*, 79 (1996) 1793–1800.

[41] University of Cambridge, *Austenite and Ferrite (crystallography and Diffraction)* (2003).

[42] B. Zuo, N. Saraswati, T. Sritharan, H.H. Hng, Production and annealing of nanocrystalline Fe-Si and Fe-Si-Al alloy powders, *Materials Science and Engineering A*, 371 (2004) 210–216.

[43] Ivan Tarasov, Zakhar Popov, Maxim Visotin, Ivan Yakovlev, and

Sergey Varnakov, EPJ Web of Conferences, 185(2018) 03014

[44] Ikuo Ohnuma, Shinya Abe, Shota Shimenouchi, Toshihiro Omori, Ryosuke Kainuma, and Kiyohito Ishida, ISIJ International, 52 (2012) 540-548.

[45] R. Rebhan, M. Rohwerder, M. Stratmann, CVD of silicon and silicides on iron, Applied Surface Science, 140 (1999) 99-105.

[46] Josh Aller, Ryan Mason, Kelly Waal, Greg Tatar, Nathn Jacobson, and Paul Gannon, High-Temperature (550-700°C) Chlorosilane Interactions with Iron. Journal of The Electrochemical Society, 163 (2016) C666-C674.

[47] Sung-Yul Lee, Gun-young Chung, Siliconizing of Bonded Couple between Fe-5.8at.%Si and (Si wafer or Fe-Si Alloy), Journal of the Korean Society of Marine Engineers, 27 (2003) 134-144.

[48] Shaoqing Wang, Peng Zhou, Weibin Zhang, Senlin Cui, Lijung Zhang, Ming Yin, Dandan Liu, Honghui Xu, Shuhong Liu, Yong Du, Atomic mobility and diffusivity of bcc\_A2 phase in the Fe-X (X= Cu, Si, Zn) systems, Computer Coupling of Phase Diagram and Thermochemistry, 36 (2012) 127-134.

## 요약 (국문 초록)

### Fe-Si 전기강판 재료의 표면핵생성 유도에 의한 cube-on-face 집합조직 형성에 관한 연구

전기강판 재료는 크게 방향성과 무방향성으로 분류할 수 있다. 방향성 전기강판의 경우 일반적으로 변압기용 소재로 쓰이며 소재의 특성 향상을 위해  $\{110\}\langle 001\rangle$ 의 특정 방위를 형성하고 있는 Goss 집합조직을 성장시켜 그 특성을 향상시킬 수 있다. 반면 무방향성 전기강판의 경우 일반적으로 회전하는 모터나 발전기용 소재로 사용된다. 일반적으로 철강재료의 자기적 특성은 소재의 조성, 미세조직, 집합조직등을 통하여 제어 가능하다. 특히 무방향성 전기강판의 경우 현재까지는 소재의 조성을 제어하는 방법으로 특성을 최적화 하는 방법에 집중되어 있다. Cube-on-face 집합조직은 무방향성 전기강판 소재에서는 꿈의 소재로 불리고 있으며  $\{100\}\langle 0vw\rangle$ 의 방위를 갖기 때문에 회전하는 회전방향으로의 매우 우수한 자기적 특성을 나타낸다. 하지만 현재까지 집합조직을 개선하여 특성을 향상시키는 연구에 대해서는 진전이 이루어지지 않은 실정이다.

본 연구에서는 상변태 열처리 시 시편에 가해지는 응력에 의하여 집합조직의 특성이 변형된다는 것을 확인하였다. 특히 감마  $\rightarrow$  알파 상변태 시 시편과 맞닿아 있는 물질과의 열팽창계수 차이가 있을 경우 시편에 아주 강한 cube-on-face 집합조직이 형성된다는 사실을 실험적으로 확인하였고, 이 결과들로부터 감마  $\rightarrow$  알파 상변태 시 열팽창계수의 차이에 의하여 표면에서 생성되는 알파상의 핵생성 장벽이 낮아지며 이때 생성되는 알파상의 방위가  $\{100\}\langle 0vw\rangle$ 를 형성시킬 것이라는 가설을 세울 수 있었고 표면 핵생성이 cube-on-face 집합조직 형성에 핵심 요소임을 확인하였다.

시편에 가해지는 응력 효과를 이용할 수 있는 방법으로, 시편의 자중을 이용하여 감마  $\rightarrow$  알파 상변태 시 크립 변형에 의해 시편에 인장을 가해줄 수 있는 방법을 고안하였고 이를 이용하여 Fe-2wt%Si-1wt%Ni의 조성까지 강력한 cube-on-face 집합조직을

형성시키는데 성공하였다.

또한, 실제 공정에 적용할 수 있는 가능성을 높이기 위한 새로운 방법으로 배치식 열처리를 고려하였고 이를 고려하여 시편을 세운 방향으로 시편에 압축 응력을 가한 상태에서 감마 → 알파 상변태 열처리 방법을 고안하였다. 이 상태에서는 시편의 세운 길이만큼의 단축 응력이 발생하는데, 이 방법을 이용하여 Fe-2wt%Si-1wt%Ni의 조성에서 동일하게 강력한 cube-on-face 집합조직을 형성시킬 수 있었다.

전기강판재료에서는 실리콘의 함량이 증가할수록 시편의 비저항이 증가하기 때문에 에너지 손실을 줄이기 위해서는 소재의 실리콘 함량을 올리는 것이 필수적이다. 하지만 실리콘의 함량이 올라갈수록 압연 공정시 소재가 깨지기 쉬워지기 때문에 실제 공정에서는 약 3wt%Si 내외로 생산이 되고 있다. 이러한 실리콘 소재의 장점은 극대화 하고 소재의 가공성에 대한 단점을 최소화 하기 위하여 실리콘의 확산을 이용한 새로운 cube-on-face texture 형성 방법을 고안하였다. 이를 이용하여 10.69wt%Si 조성을 형성하면서 81.9%의 {100} <0vw> 집합조직 형성시킬 수 있었으며 이 방법을 이용하여 최대 96.8%를 갖는 강력한 cube-on-face 집합조직을 형성시키는데 성공하였다.

**주요어** : Fe-Si 전기강판; 상변태; 표면핵생성; Cube-on-face 집합조직; 자기적 특성

**학번**: 2018-34848